Integrated water cooling for HIFU prostate ablation

By:
Ting Yan
Student number: 4038800

Supervisor:
Prof. Dr. Ir. Ronald Dekker (Philips Research Eindhoven/TU Delft)

M.Sc. thesis in Electrical Engineering (Microelectronics)
Delft University of Technology
Philips Research Eindhoven

TU Delft

Challenge the future

Table of Contents

Chapter 1 Introduction 1

1.1 Medical background 1

1.2 HIFU as treatment 2

1.3 Project objectives 3

Chapter 2 Theory of Heat Transfer 5

2.1 Heat transfer 5

2.1.1 Conduction 5

2.1.2 Convection 5

2.1.3 Radiation 6

2.2 Micro fluid--Single Phase Flow convection 6

2.2.1 Reynolds number 6

2.2.2 Continuum level of fluid transfer phenomenon 7

2.2.3 Pressure drop in a rectangular channel 9

Chapter 3 Design and Simulation 11

3.1 Overview 11

3.2 Design of the chip 13

3.2.1 The aluminum heater design 13

3.2.2 Backside Micro-channels Design 14

3.3 COMSOL Simulation 16

Chapter 4 Practical implementation 20

4.1 Fabrication sequences 20

4.2 Full process overview 21

4.2.1 The oxidation steps 22

4.2.2 Patterning of the backside oxide layers 22

4.2.3 Fabrication of the heater structures on the frontside 22

4.2.4 DRIE etching of the micro-channels 23

4.2.5 Discussion 25

4.3 Packaging and interconnections 28

4.3.1 Chip level bonding 29

4.3.2 Wafer level bonding 30

4.3.3 The electrical interconnections 35

Chapter 5 Experimental setup and results 38

5.1 Cooling capacity experiment....................38
5.1.1 Experimental setup....................38
5.1.2 Experimental result....................40
5.2 MRI guide HIFU experiments....................48
Chapter 6 Conclusions and recommendations....................51
Reference....................53
Acknowledgment....................55
Appendix A- Detailed fabrication sequence....................56
Appendix B- Detailed process flow of BCB wafer bonding....................58

Chapter 1 Introduction

1.1 Medical background

As shown in Fig. 1.1, the prostate is a gland found only in the male reproductive system, whose position is just below the bladder and in front of the rectum. The tube that carries urine (the urethra) runs through the center of the prostate. One function of prostate is to help control urination by pressing directly against the part of urethra that it surrounds. The main function of the prostate is to produce some of the fluid that protects and nourishes the sperm [1-2].

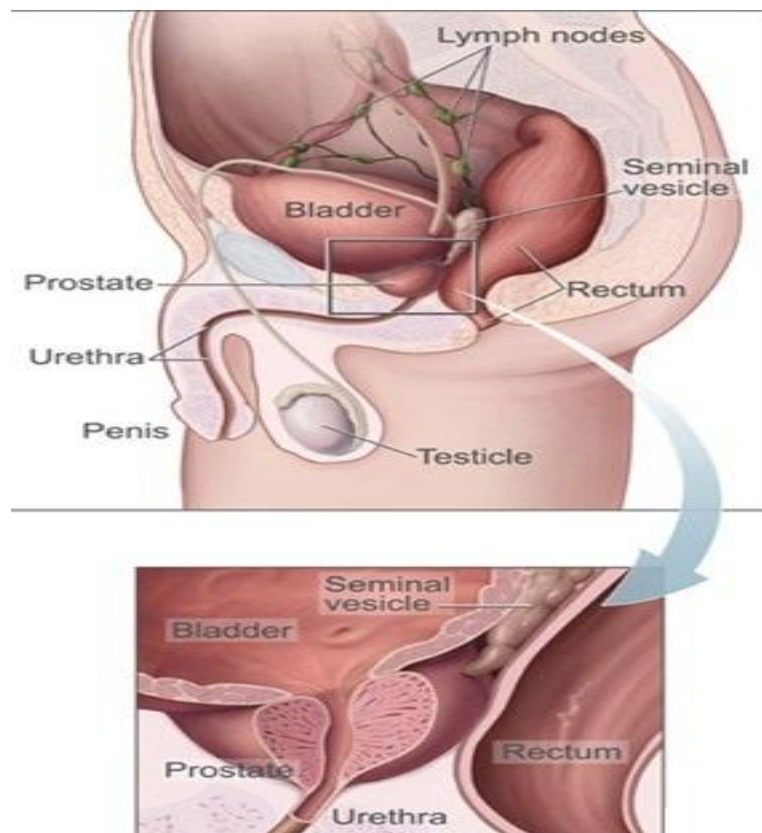

Figure 1.1- The position of prostate gland and nearby organs (adapter from [1])

The size of the prostate varies with age. In younger men, it is the size of a walnut and weighs around one ounce (< 30g), but it can be much larger in older men. This hormone-related enlargement with aging is called benign prostatic hyperplasia (BPH), which is a growth of non-cancerous cells. The enlargement results in a gradual squeezing of the urethra, which leads to the difficulties in urinating, weak urinary stream, or prostatitis. In some other cases, if malignant cells in the prostate grow and can't be controlled, it will damage surrounding tissue and interfere with the normal

function of the prostate. In this condition, prostate cancer occurs. The cells can then spread to other parts of the body, such as bones and lymph node [3].

Prostate cancer is the most common non-skin cancer in men and the third leading cause of male cancer deaths. And the impact of BPH is also significant. By the age of 80, up to 90% of male population will experience BPH [4]. So the treatment for BPH and prostate cancer is very important. There are numerous treatment options for prostate cancer and BPH, such as Hormone Therapy, Radical Prostatectomy, and Radiation Therapy [9]. Each treatment has its benefits and drawbacks. It means patients and their physicians need to weigh all the factors as they search for the best treatment option. Although there are many treatments available, patients are still waiting for a reliable and minimally invasive alternative to open surgery or external beam radiation. As a candidate alternative HIFU has been developed. It has very attractive features and promising initial results.

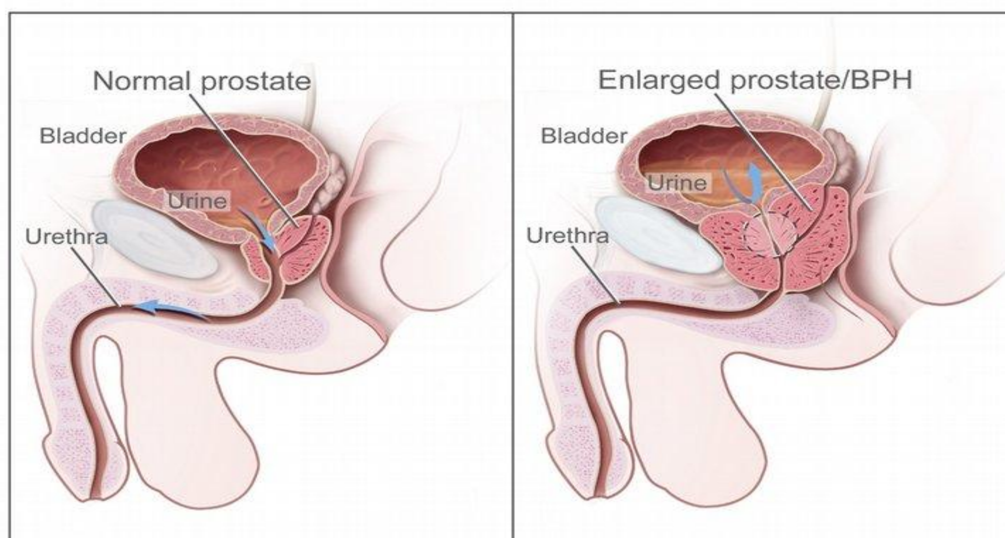

Figure 1.2- The comparison between normal prostate and enlarged prostate (adapter from [2]).

1.2 HIFU as treatment

High Intensity Focused Ultrasound, or HIFU, is an innovation medical therapy to heat and destroy tissue rapidly and precisely. HIFU relies on the same principles as conventional ultrasound. It can propagate harmlessly through living tissue, and if the ultrasound beam carries sufficient energy and is brought into a tight focus, the energy within the focal volume can cause a local rise in temperature of sufficient magnitude to cause tissue necrosis (a "lesion") (Fig. 1.3) [5-7].

Compared to the other traditional treatments, HIFU is a minimally invasive therapy

that does not use ionizing radiation, which can be potentially harmful. One of important applications of HIFU is MRI-guided HIFU system which can offer excellent soft tissue contrast, 3D imaging capabilities, and noninvasive temperature measurement techniques [8].

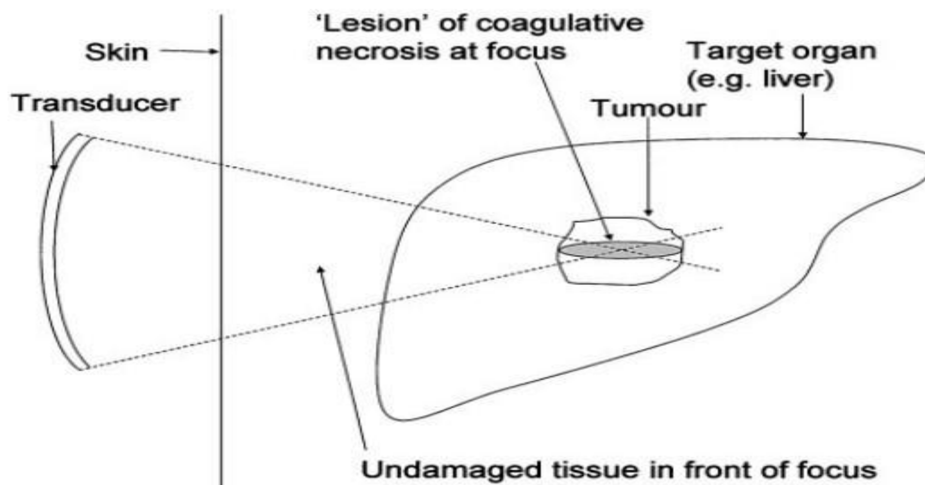

Figure 1.3- The schematic representation of HIFU lesion production (adapted from [5]).

1.3 Project objectives

In the ideal condition, when HIFU is focused at a specific location, the temperature of that part rises to almost 90 degrees Celsius in a matter of seconds. Only tissue at the "focal point" is destroyed and any tissue outside of the focal point should remain unharmed. This ideal condition, as shown in Fig. 1.3, assumes the HIFU device is placed out of human body. However, in reality it is very difficult to focus enough energy in the tumor with an external ultrasound source. An alternative is to insert the ultrasound source through the penis into the prostate directly. A problem here is that, due to the limited efficiency of the ultrasound transducers, energy is also dissipated in the transducer which can result in unacceptable heating. The maximum temperature which normal tissue in the human body can endure is around 42 degrees Celsius. If the maximum surface temperature is higher than this, the surrounding tissue can be damaged. One possible solution is to remove this heat by water cooling.

In this project, we try to find a suitable way to integrate water cooling in a micro fabricated HIFU device, to remove unwanted heat and ensure proper functionality of the medical device. The water cooling is implemented by etching a system of micro fluidic channels in the backside of the device.

The remaining chapters of this thesis are arranged as follows: in Chapter 2, a theory review of heat transfer and micro fluidics is provided. Chapter 3 discusses the design

geometries and the FEM simulations. In Chapter 4, the practical fabrication process is described and the results of fabrication are illustrated. Finally, in Chapter 5 the results of cooling capacity tests on the device are presented and compared with the simulations, followed by conclusions and recommendations for future work.

Chapter 2 Theory of Heat Transfer

2.1 Heat transfer

The theory of heat transfer seeks to predict the energy transfer that takes place between objects as a result of a temperature difference of these objects. There are three modes of heat transfer: conduction, convection and radiation [10].

2.1.1 Conduction

Conduction can be viewed as the transfer of energy from the high temperature region to the low temperature region when a temperature gradient exists in a body. The heat flux vector ($\vec{q}$ $[Wm^{-2}]$) is the heat transfer rate per unit area perpendicular to the direction of heat transfer and is proportional to the temperature gradient [11]:

$$\vec{q} = -k\nabla T \qquad (1)$$

The positive constant k is called the thermal conductivity of the material ($[Wm^{-1}K^{-1}]$), and the minus sign is inserted as a consequence of the fact that heat is transferred in the direction of decreasing temperature.

2.1.2 Convection

Convection is the heat transfer by mass motion of a fluid (such as air or water) when the heated fluid is caused to move away from the source of heat, carrying energy with it[12].

There are two major types of heat convection:

1. Natural convection: when the fluid motion is caused by buoyancy forces that result from the density variations due to variations of temperature in the fluid.
2. Forced convection: when the fluid is forced to flow over the surface by external source, creating an artificially induced convection current.

For our project of micro-channel cooling, heat transfer due to convection between a fluid in motion and a boundary surface has to be considered. There are two kinds of boundary layer [13]:

1. Hydrodynamic boundary layer. A consequence of fluid flow is the development of a region in the fluid through which the velocity varies from zero to a finite value u_∞, associated with the bulk flow. This region is known as the hydrodynamic boundary layer.

2. Thermal boundary layer. If the surface and flow temperature varies from T_s at inlet to T_∞ in the outer flow, this region is called as thermal boundary layer.

The heat flux due to convection is given [11] by Newton's law of cooling:

$$q = \bar{h}\ (T_{body} - T_\infty) \qquad (2)$$

where h is the convection heat transfer coefficient. The bar over h indicates that it is an average over the surface of the body. Without the bar, h denotes the "local" value of the heat transfer coefficient at a point on the surface. The units of h are W/(m^2 K). In general, this value h depends on conditions in the boundary layer, which are influenced by surface geometry, the nature of the fluid motion and an assortment of fluid thermodynamic and transport properties.

2.1.3 Radiation

In contrast to the mechanisms of conduction and convection, where energy transfer through a material medium is involved, heat may also be transferred through regions where a perfect vacuum exists. If the mechanism in this case is the result of a temperature difference, this is called thermal radiation.

All bodies and surfaces constantly emit thermal radiation and absorb or reflect incident radiation. The flux of energy radiating from a body is commonly designated $e_b(T)$, [W/m^2]. For an ideal radiator or blackbody, emissive power can be prescribed by the Stefan-Boltzmann law,

$$e_b(T) = \sigma T_s^4 \qquad (3)$$

where T_s is the absolute temperature [K] of the surface and σ is the Stefan-Boltzmann constant ($\sigma = 5.67 \times 10^{-8} W/m^2K^4$).

The heat flux emitted by a real surface is less than that of a blackbody at the same temperature and is given by

$$e_b(T) = \varepsilon\sigma T_s^4 \qquad (4)$$

where ε is a radiative property of the surface termed the emissivity. With values in the range $0 \le \varepsilon \le 1$, ε depends on strongly on the surface material, color, degree of oxidation and the presence of coatings.

2.2 Micro fluid--Single Phase Flow convection

2.2.1 Reynolds number

The Reynolds number is the most important dimensionless number in fluid mechanics, which represents the ration of importance of inertial effects in the flow to viscous effects in the flow. "Inertia" is the property of an object to remain at a constant velocity, unless an outside force acts on it. An object with a large inertia will resist strongly to a change in velocity, in other words it is difficult to start or stop its movement. An object with small inertia, on the other hand, will almost

instantaneously start or stop when acted upon by some external or internally generated force. “Viscosity” is the resistance of a fluid to flow under the influence of an applied external force. It is the source of drag on objects moving through the fluid. For such an object, inertia hence strives to keep the object going, whereas viscosity tries to stop it [14].

The Reynolds number, Re is given by [14]

$$\mathrm{Re} = \frac{\rho V D_h}{\mu} = \frac{V D_h}{\upsilon} \tag{5}$$

Where ρ is density, V is velocity, and μ is dynamic viscosity of the fluid, and D_h is the hydraulic diameter of the micro-channel. The hydraulic diameter can be given by [15]:

$$D_h = \frac{4\ \text{Cross Secetion Area}}{\text{perimeter}} = \frac{4S}{P} = \frac{2wh}{w+h} \tag{6}$$

with w and h the width and height of channel respectively, as shown in Figure 2.1.

For macroscopic channels ($D_h > 1\text{mm}$) with single direction, Laminar flow occurs for Reynolds number smaller than 2000. Turbulent flow occurs for Reynolds number higher than 2300. However in the case of micro-channel, the Reynolds number for transition between laminar and turbulent flow is still not well known. Several investigations and experiments show the transition from laminar to turbulent flow occurs at much smaller Reynolds numbers.

Figure 2.1- The cross section of single micro-channel

2.2.2 Continuum level of fluid transfer phenomenon

Depending on the length scale, transport phenomena of fluid flow in micro channels can be described at two basic levels, either the molecular level or the continuum level. Molecular level models involve transport phenomenon in the range from one nanometer to one micrometer. The continuum model is used if the length scale lies between micrometers to centimeters range [16].

The length of all channels in this project is in the micrometer range, which can be treated at the continuum level.

At continuum level, transport phenomena can be described by a set of conservation equations for mass, momentum, and energy. There are three basic conservation equations:

(I) Conservation of mass: continuity equations

Conservation of mass means, in any steady state processes, that the rate at which mass enters a system has to be equal to the rate at which mass leaves the system.

The continuity equation is given by:

$$\frac{\partial \rho}{\partial t} + \nabla \cdot (\rho\, \mathbf{u}) = 0 \qquad (7)$$

where ∇ is the napla operator and $\mathbf{u}$=(u,v,w) is the velocity vector.

This equation is reduced to the form

$$\nabla \mathbf{u} = 0 \qquad (8)$$

for incompressible liquids. It means that the divergence of the fluid velocity is zero.

(II) Conservation of momentum: Newton's second law or Navier-Stokes equations

Conservation of momentum is described by Newton's second law:

$$\rho \frac{D\mathbf{u}}{Dt} = f = f_{body} + f_{surf} \qquad (9)$$

The left hand side of the equation represents the acceleration force, while the right hand side consists of force per unit volume on a fluid particle. $\frac{D}{Dt}$ is the total derivative operator.

For velocity field $\mathbf{u}$, the total derivative operator is given by:

$$\frac{D\mathbf{u}}{Dt} = \frac{\partial \mathbf{u}}{\partial t} + \mathbf{u}\nabla\mathbf{u} \qquad (10)$$

In micro scale surface forces such as viscous force, electrostatic force, or surface stress are dominant over body forces. Common body forces are gravity, electromagnetic forces and inertial forces. If the only body force is the gravity and surface forces are caused by a pressure gradient and viscous force and both density and viscosity are constant, the Navier-Stokes equation can be reduced to:

$$\rho\left(\frac{\partial \mathbf{u}}{\partial t} + \mathbf{u}\nabla\mathbf{u}\right) = \rho\mathbf{g} - \nabla p + \eta\nabla^2\mathbf{u} \qquad (11)$$

where $\rho\mathbf{g}$ is force due to gravity, ∇p is pressure gradient and $\eta\nabla^2\mathbf{u}$ is friction force.

When we neglect the force due to gravity in micro channels, the steady flow in above equation can be written as:

$$\rho\left(\frac{\partial \mathbf{u}}{\partial t}+\mathbf{u}\nabla\mathbf{u}\right)=-\nabla p+\eta\nabla^2\mathbf{u} \tag{12}$$

(III) Conservation of energy: first law of thermodynamics

The conservation of energy is governed by the first law of thermodynamics:

$$dQ+dW=dE_{total} \tag{13}$$

which means, the change of the total energy in a system is equal to the sum of the heat and work added to the system. The equation can be stated as:

$$\rho c_p\frac{DT}{Dt}=\beta T\frac{Dp}{Dt}+\mathrm{div}(k\nabla T)+\phi \tag{14}$$

where c_p is the specific heat at constant pressure, $\beta=-\frac{1}{\rho}(\frac{\partial\rho}{\partial T})_p$ is the thermal expansion coefficient, k is thermal conductivity and ϕ is the dissipation function.

For an incompressible flow, a constant thermal conductivity and ignoring the kinetic energy change, the energy equation can be simplified to the heat-convection equation:

$$\rho c_p\frac{DT}{Dt}=k\nabla^2 T \tag{15}$$

2.2.3 Pressure drop in a rectangular channel

The pressure drop in a rectangular channel can be calculated using [18]:

$$\Delta p=\rho g\left(f\frac{L}{D_h}\frac{V^2}{2g}+\sum K\right) \tag{16}$$

Here, g is the gravitational acceleration, L is the length of the channel and V is the mean velocity. The friction factor f yields f=64/Re for laminar flows, for turbulent flows it can be looked up in the so called Moody chart (Figure 2.2). This chart clearly shows that turbulent flows cause larger pressure drops than laminar flows. The first term in Eqn. 16 represents the pressure drop due to friction forces on the walls of the channel. The second term accounts for additional (minor) losses due to e.g. pipe entrance or exit, and sudden/gradual expansion or compression. Normally, we neglected the second term.

The Moody chart is designed for circular ducts, for rectangular ducts an effective diameter and effective Reynolds number should be calculated as:

$$D_{eff}=\frac{64}{fRe_{D_h}}D_h \tag{17}$$

$$\mathrm{Re}_{D_{eff}} = \frac{VD_{eff}}{\nu} \quad (18)$$

Here, fRe_{Dh} is the laminar friction constant for different aspect ratios of the channel; ε is the surface roughness height.

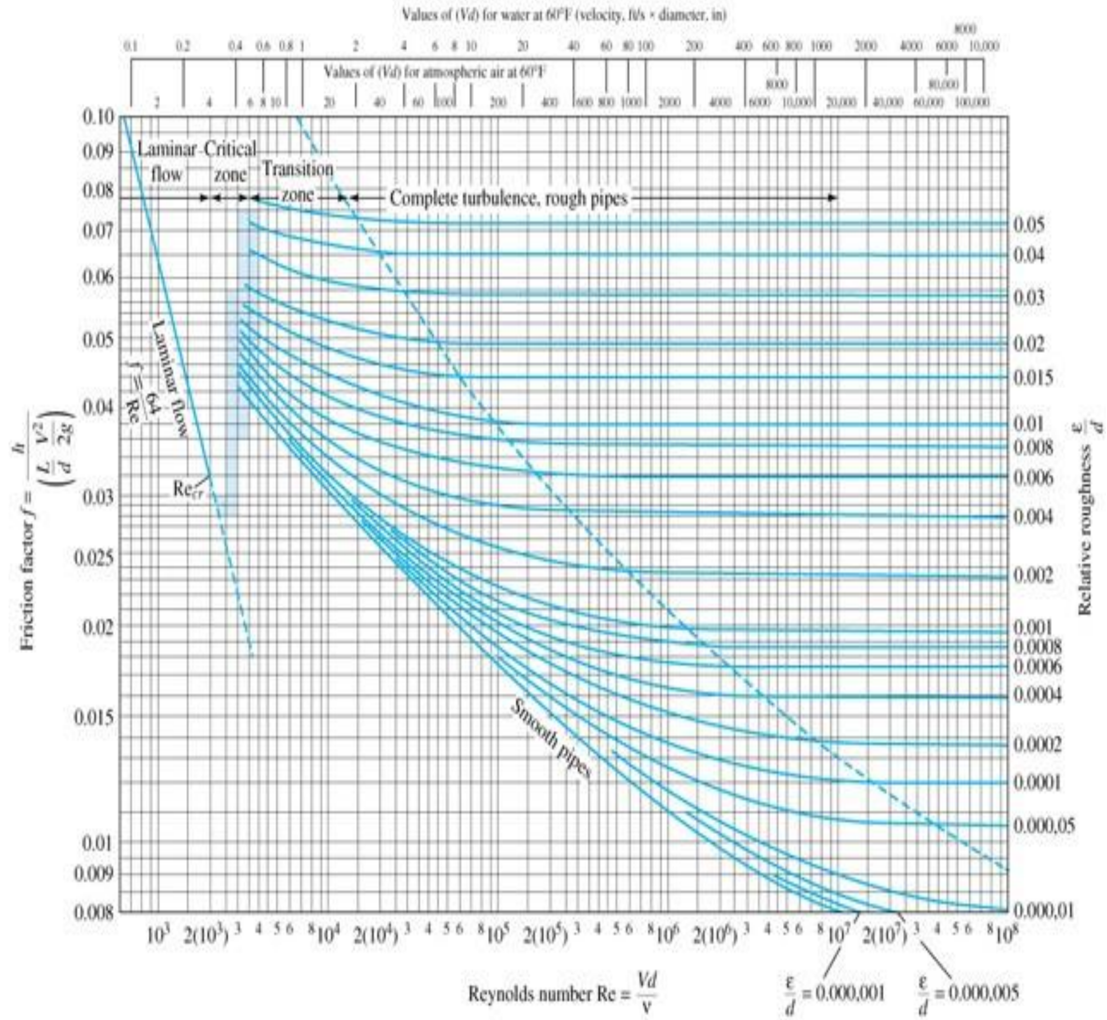

Figure 2.2: The Moody chart for pipe friction with smooth and rough walls (adapted from [17]).

Chapter 3 Design and Simulation

3.1 Overview

The length of the current HIFU device is 5cm and the width is 5mm. It is not necessary to process a real HIFU ultra-sound device just to study the efficiency of the water cooling. Instead a simple device only consisting of aluminum heaters was fabricated with the same size as the HIFU device, generating the same power of 20 Watt. Trenches are etched in the backside of silicon wafer to form the various micro-channels. In the simplest design the entrance and exit fluidic connections are placed at the opposite ends of device. However, when the device is placed at the tip of an ablation catheter, the entrance and exit ports of the microgroove channels should be placed at the same end of the device. So the real device U-shaped micro channels are used (Fig. 3.1). To seal the micro channels two identical devices are glued back to back. Figure 3.2 gives a schematic example of device used in the experiments described in this thesis.

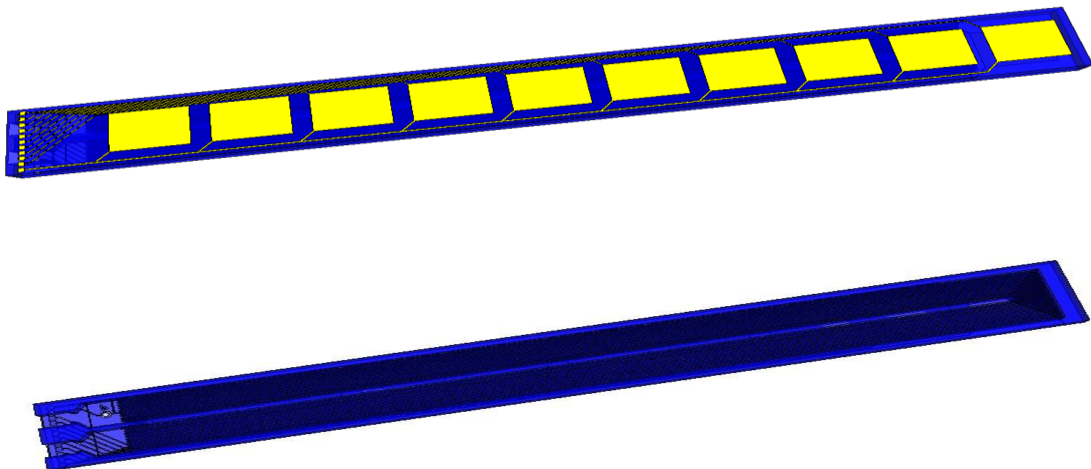

Figure 3.1- The schematic overview of the single strip HIFU device.

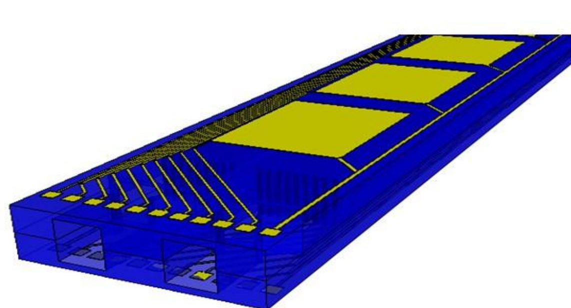

Figure 3.2- Schematic overview of the double strip HIFU device.

In this project, there are two types of designs which we use for different experimental purposes. To avoid misunderstanding, we distinguish them as “real cooling device” and “test cooling device”.

The "real cooling device" (Fig. 3.3-A) is designed to demonstrate the packaging water cooled HIFU device on the tip of an ablation catheter. This test device will be used in an MRI test. It has exactly the same size and shape as the real HIFU device and has the fluidic and electrical connections located at the same side. The "test cooling device" is designed for use in the experimental setup where the cooling measured. To simplify the mounting of the device in the experimental setup the electrical connections are designed on one end of the device, while the fluidic connections are placed at the opposite side. In this way the electrical connections are well separated from the fluidic connections. Additionally the length of entrance/exit channel (L_e) is extended to guarantee that a small tip of a syringe or a tube can be fixed inside the port without blocking a channel.

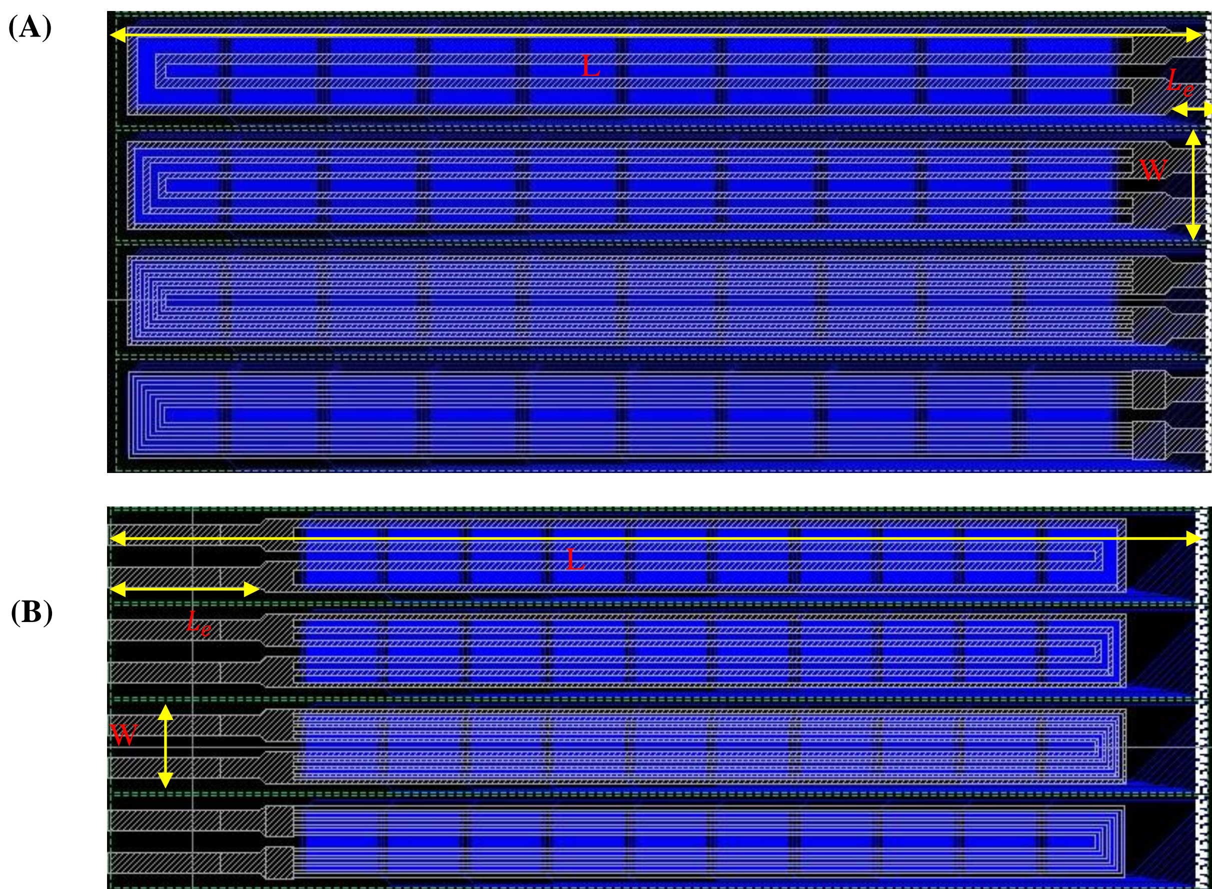

Figure 3.3-The different geometries requirement of real and test cooling device.
(A) real cooling device- L_e=2.2 mm, L=5 cm, W=5 mm
(B) test cooling device- L_e=8.2 mm, L= 6 cm, W=5 mm

3.2 Design of the chip

3.2.1 The aluminum heater design

A real HIFU device consists of ten ultra-sound transducers which can be individually switched on or off depending on the type of therapy needed. To simulate the power generated by HIFU transducers, ten meander-shaped aluminum heaters simulating the ultra-sound transducers (Fig. 3.4) are fabricated on the front side of the device. Since the future HIFU transducers can be used in various combinations to generate different power energy in the treatment, the ten aluminum heaters are designed in a shunt configuration. For the heaters are controlled by an external switch box with ten switches corresponding to each heater. Another reason that we choose a shunt connection is to reduce the failures from fabrication. In a serial connection, one broken heater would make the whole chip useless, so the shunt connection is much safer for fragile heaters.

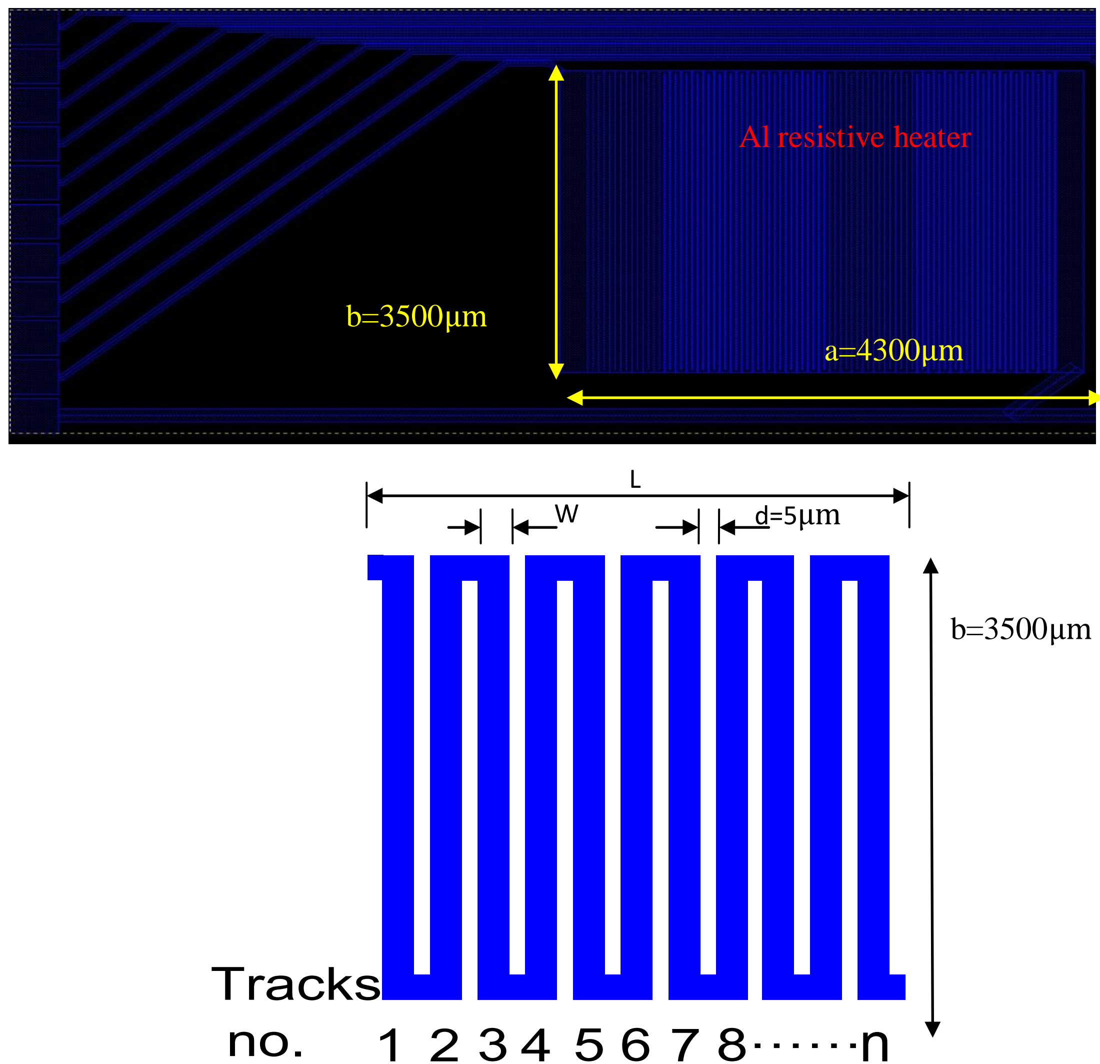

Figure 3.4- The geometry of aluminum heaters.

The resistance [19] of the Al heater is determined by:

$$R = R_s * \frac{L}{W} \tag{3.1}$$

where R_s is the sheet resistance, L is the total length of the aluminum tracks and W is the width of one track. Since R_s depends on the thickness of the Al layer as well as on the deposition conditions. For the 0.7 μm thick layer of aluminum used in our experiments a sheet resistance of approximately 60 $m\Omega/_{sq}$ was used. Since the power dissipated by one aluminum heater is P_{unit}=20 Watt/10=2 Watt. With a maximum reasonable voltage U_{max} =30 V, the maximum resistance of the heater should be:

$$P_{max} = {U_{max}}^2/P_{unit} = 30^2/2 = 450\Omega.$$

Besides, the total length of one heater is 4300 μm, the width of it is 3500 μm and the minimum space between two tracks is 5 μm. Therefore, the design of aluminum heater should meet both geometrical and electrical constraints:

$$W \times n + (n+1) * 5 \leq a = 4300 \text{ μm}$$
$$0.06\,\Omega/_{sq} \times \frac{n * 3500 \text{ μm } + 5 * (n+1)}{W} \leq 450\ \Omega$$

where W is practical width of an tracks and n is the number of tracks on one heater. A suitable solution for these two constraints is: W=40 μm and n=85. It means, in this design, there are 85 tracks in one heater and the practical width of each track is 40 μm (Fig. 3.4).

3.2.2 Backside Micro-channels Design

In order to get a comparable result in the cooling capacity test, the entrance and exit ports on the different chips were designed with the same geometries (Fig. 3.5). To simplify the design, the height of every channel in chip was assumed to have the same value of h= 500 μm. The maximum width of one channel has to be less than 2.5 mm, half of the total chip width. With a high aspect ratio DRIE ($\frac{Etch\ Rate_{depth}}{Etch\ Rate_{width}} = \frac{20}{1}$), the minimum width of one channel is 25μm. So, the range of channel width is from 25μm to 2.5mm.

In this range, four types of geometrical micro-channel with different contact surface area are chosen. Because of their different numbers of channel in the chip, as shown in Fig.3.6, we classify them as "2-channel chip", "3-channel chip", "5-channel chip" and "9-channel chip" .

And in this design, for the different devices (double strip), the total cross section area of water flowing (inlet) is given by:

$$A_{\text{cross section}} = n * Wc * 2h \qquad (3.2)$$

where n is number of channels in one chip and Wc is the width of one channel. The total cross sectional area of the micro channels ($A_{\text{cross section}}$) for each chip is kept constant at (0.9 mm^2). The different designs are summarized inTable3.1. By keeping $A_{\text{cross section}}$ the same for every design, we expect that also the water velocity in the channels will be the same for every design for a certain inlet flow rate. The main difference between four different designs is contact surface area for removing heat by water. This contact surface area is the total areas of the walls of micro-channels. The area of heat contact surface in different devices is: 9-channel chip > 5-channel chip > 3-channel chip> 2-channel chip.

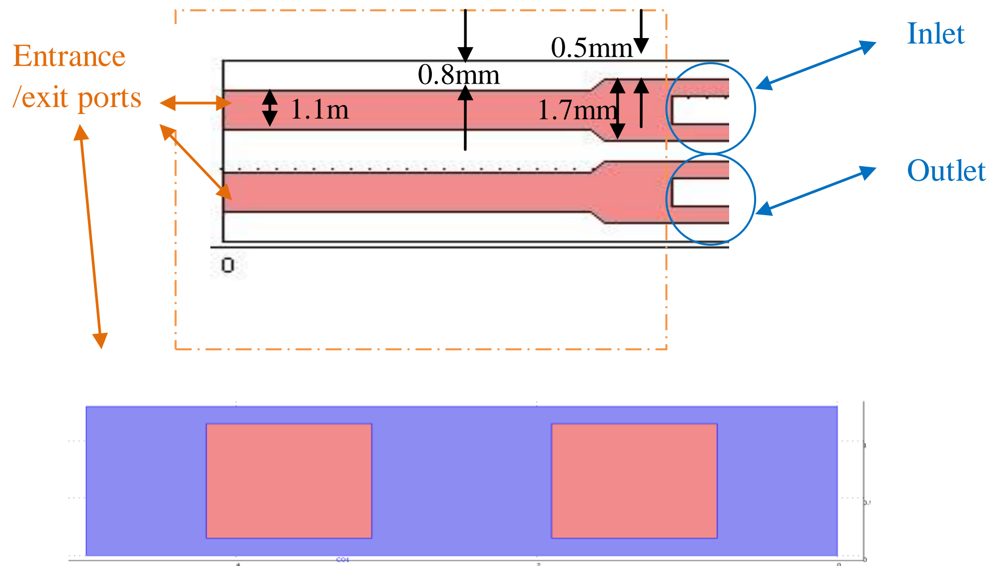

Figure 3.5-The entrance and exit ports for all chips.

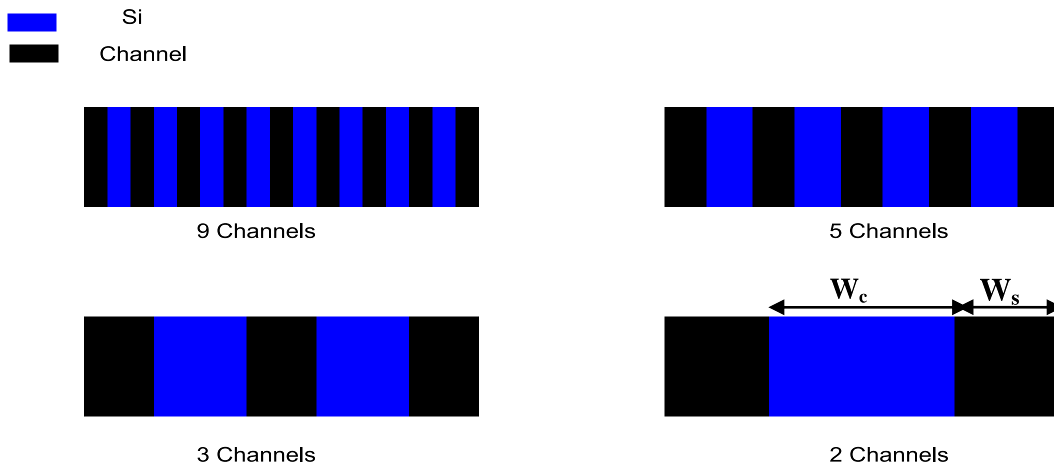

Figure 3.6- Cross Section for different design of micro-channel of inlet channels.

Table 3.1- Specification of Micro-channel (Double strips)

Design	H (μm)	W_c(μm)	W_s(μm)	$A_{cross\ section}$ (mm^2)	$A_{heat\ removed}$ (mm^2)
2-channel	1000	100	100	0.9	366.4
3-channel	1000	180	200	0.9	549.6
5-channel	1000	300	400	0.9	916
9-channel	1000	450	800	0.9	1648.8

3.3 COMSOL Simulation

For the water cooling problem, there are two coupled physical fields, heat transfer and fluid flow dynamics, which both play an important role at this project. Unfortunately it is quite difficult to obtain an analytical solution for the U-shaped channels. So, in our case, FEM simulation in COMSOL Multiphysics is helpful to provide a numerical method and ensure a basic understanding of the system.

In order to simplify the simulations, the silicon oxide layer, aluminum heater and silicon nitride passivation layer are all ignored. We assume there are only 2 sub-domains (materials) in the FEM model: silicon and water. In the simulations, the heat is generated from the ten separated silicon areas at the same position of aluminum heaters and the heat flux generated in each area is assumed to be equal and uniform. Since the media surrounding device is also treated as vacuum, it means the simulation also neglects the effect of air. Another important assumption underlying the FEM simulation model is that the flow is already fully developed and that flow is laminar.

Figure 3.7 gives an impression of the distribution of the surface temperature on the four different test devices. The initial conditions are a flow rate of 4e-7 m^3/s = 1440 mL/hr, and a power dissipation of 20 W. For the transverse direction channel structure, where the channels run from one end of the device to the other, the max surface temperature must be located on the end of channels However, in U-shaped stucture, the maximum surface temperature is located near the outlet channels side. Obviously the outlet channels side is much warmer than the inlet side.

Since a full 3D FEM simulation is time consuming; only the maximum surface temperature as a function of the flow rate and power dissipation of the 5-channel test cooling device is investigated. Figure 3.8 shows the linear relation between the maximum surface temperature and the power dissipation. Figure 3.9 shows the maximum surface temperature profile as a function of flow rate. With increasing flow rate, the maximum surface temperature decreases until it becomes constant.

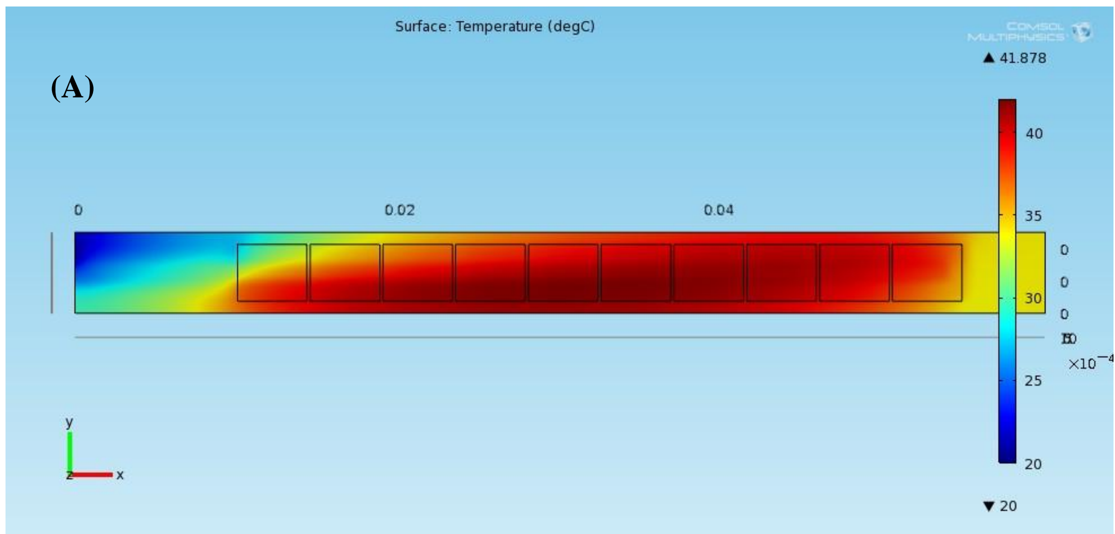
Surface: Temperature (degC)
▲ 41.878
(A)
0
0.02
0.04
40
35
30
25
20
▼ 20
y
x

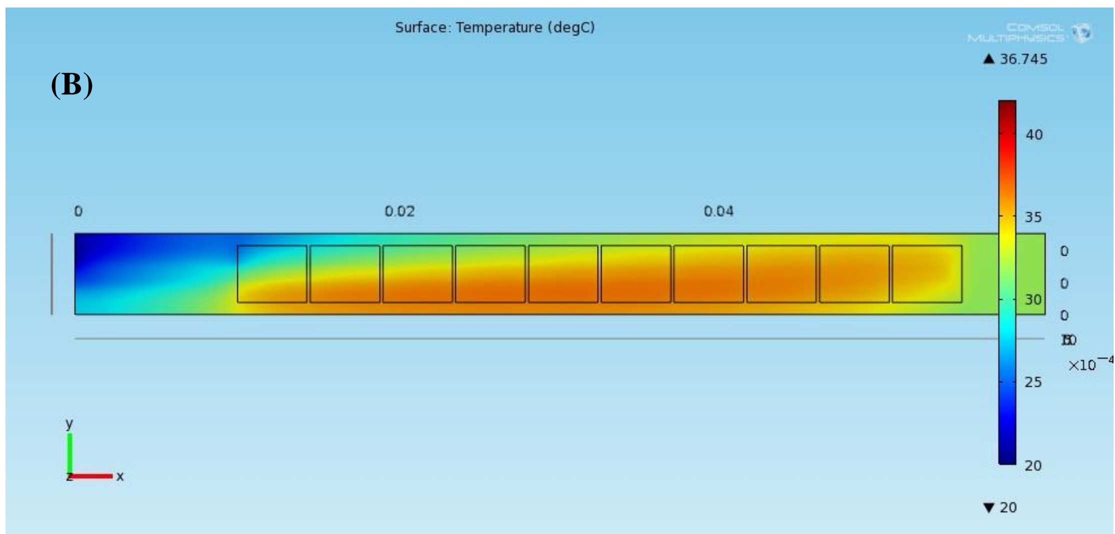
Surface: Temperature (degC)
▲ 36.745
(B)
0
0.02
0.04
40
35
30
25
20
▼ 20
y
x

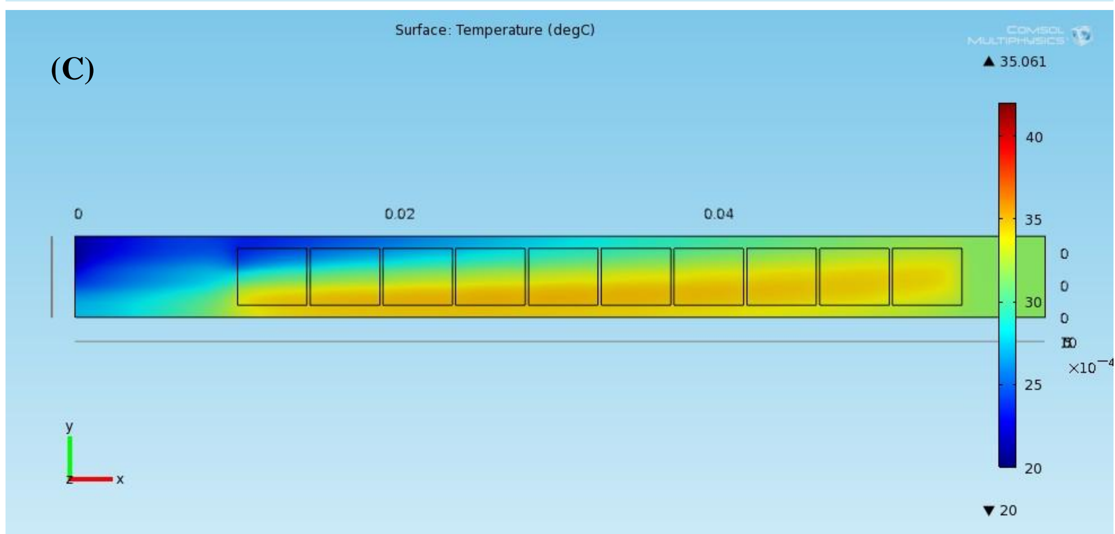
Surface: Temperature (degC)
▲ 35.061
(C)
0
0.02
0.04
40
35
30
25
20
▼ 20
y
x

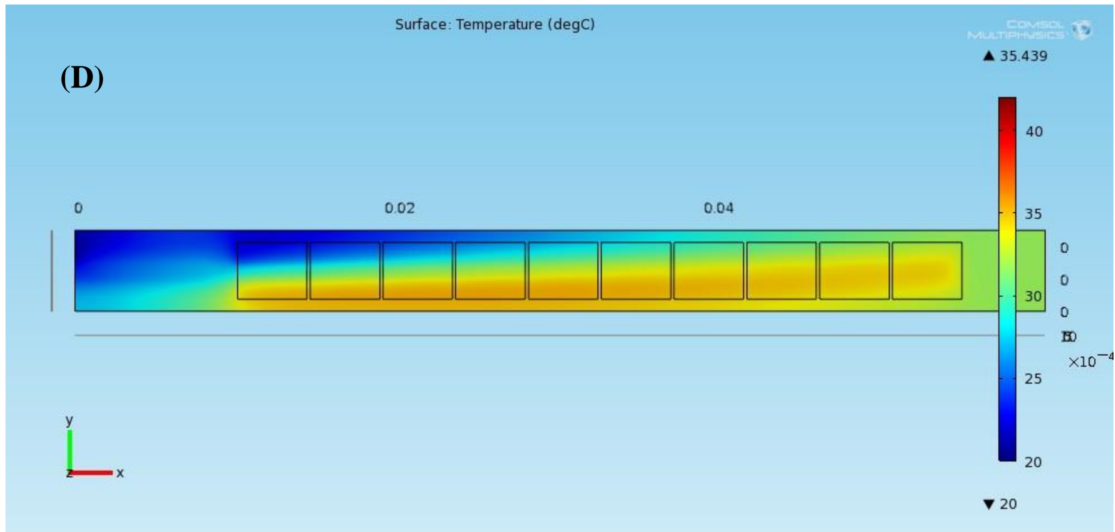

Figure 3.7- Top view of surface temperature distribution results from 3D FEM simulation on the micro-channel cooling devices with a dissipated power of 20W and flow rate at 1440ML/hr.

(A): 2-channel test cooling device; (B): 3-channel test cooling device; (C): 5-channel test cooling device; (D): 9-channel test cooling device;

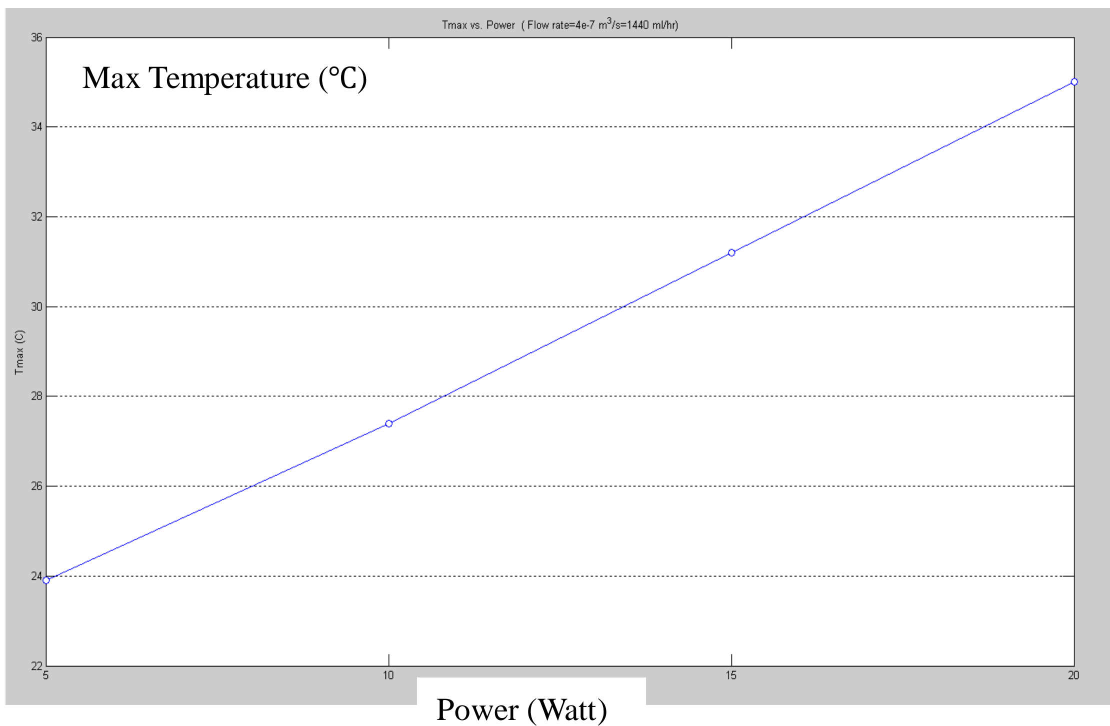

Figure 3.8- The FEM simulation: maximum surface temperature on the 5-channel cooling device as a function of the dissipation power for a flow rate of 1440mL/hr.

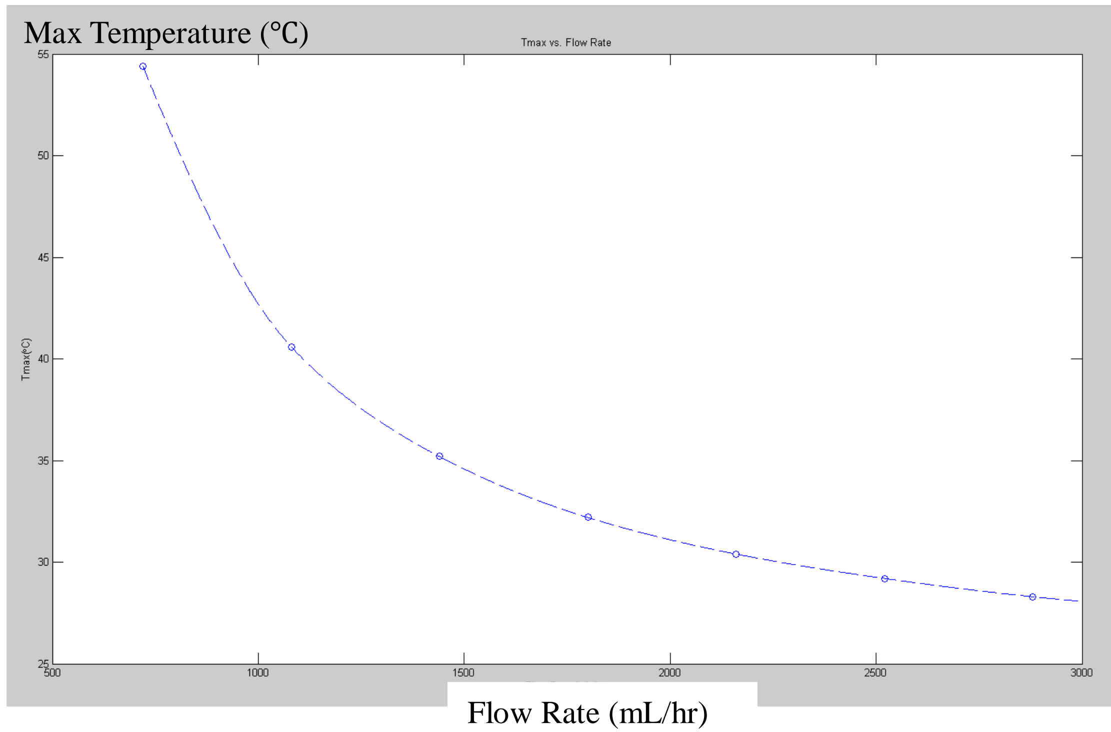

Figure 3.9- The FEM simulation: maximum surface temperature on the 5-channel cooling device as a function of the flow rate for a dissipated power of 20W

Chapter 4 Practical implementation

4.1 Fabrication sequences

In order to achieve structures on both sides of the silicon wafer, two different fabrication sequences for the micro-channel cooling device have been considered (Fig. 4.1).

(1) The aluminum heaters and the silicon nitride scratch protection layer on the front side of wafer are fabricated first. Next the backside channel pattern is defined and finally the backside channels are DRIE etched.

(2) The channel pattern on the backside is defined first. Then the heater and nitride scratch protection layer on the front side are fabricated. Finally, the silicon backside channels are DRIE etched.

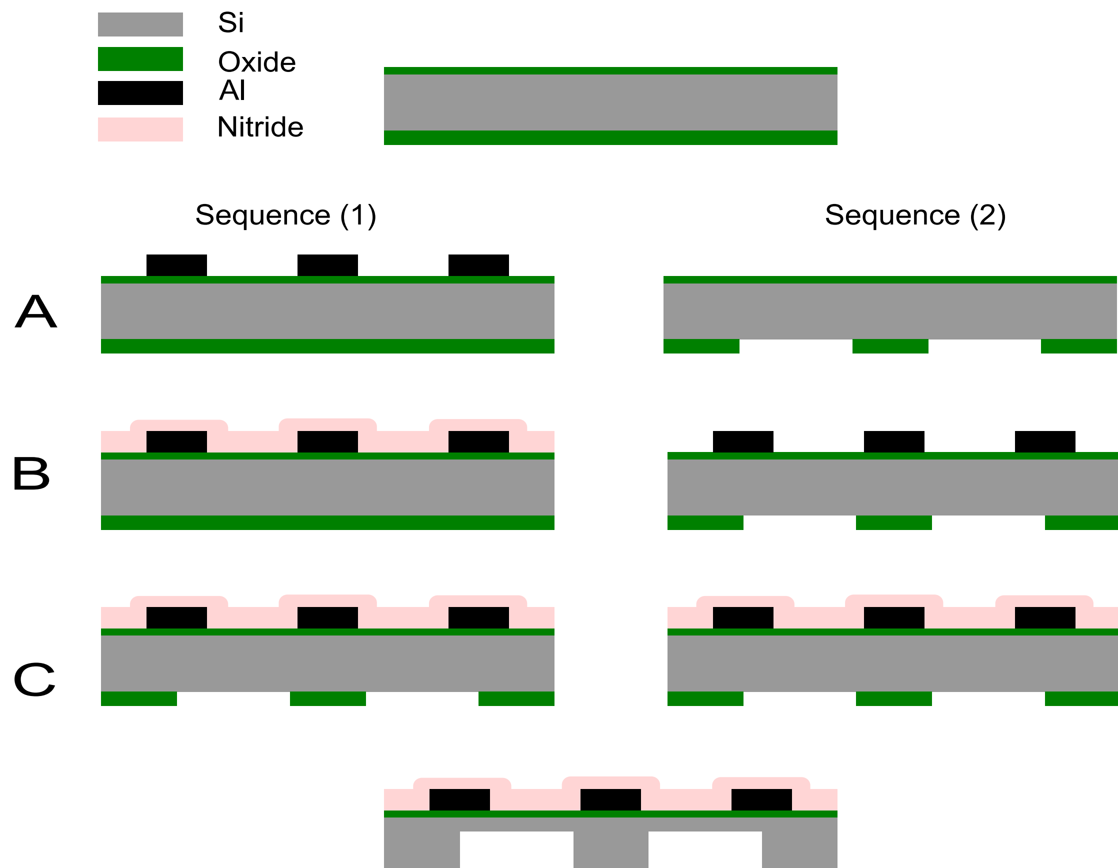

Figure 4.1- Different sequences to fabricate the double sided structures on the wafer.

Compared these two sequences, the second one can offer a better result, since it may reduce the risk of fragile front side patterns being contaminated by process in the backside fabrication. So, in this project, we prefer to adopt the second sequence to fabricate wafers.

4.2 Full process overview

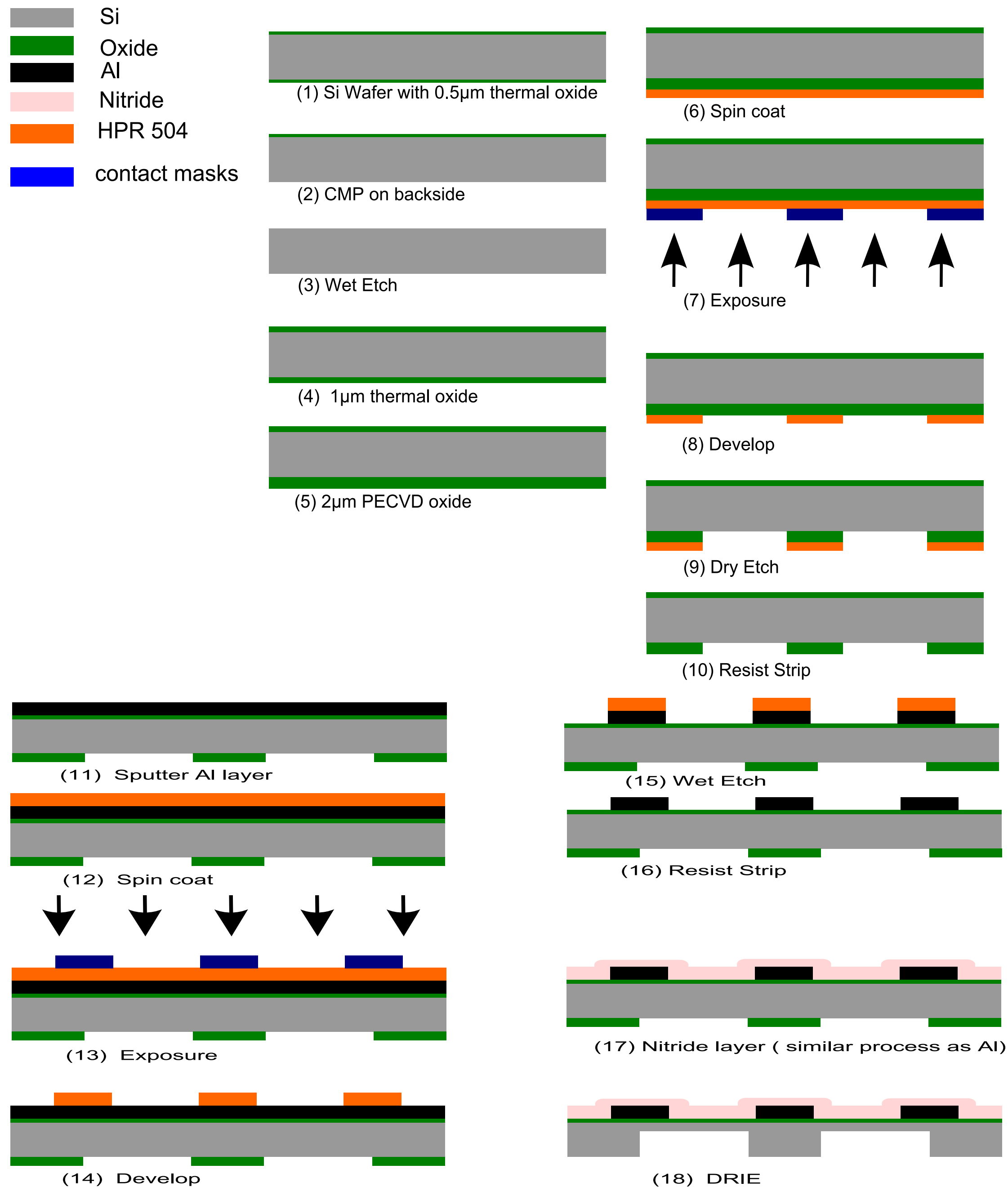

Figure 4.2- The important steps to fabricate wafers

The full process for fabrication of the wafers is completed by several steps, which are shown in the Fig. 4.2. Roughly, these steps can be divided into four parts: (1) oxidation, (2) patterning of the micro channels on backside, (3) fabrication of the heater structures on front side of the wafer, and finally (4) DRIE of the micro channels. Each part will be explained in more detail in the following sections and every detailed step can be found in Appendix A. Finally several processing issues and improvements will be discussed at the end of this section.

4.2.1 The oxidation steps

The full process started with a 6-inch silicon wafer provided with a 0.5 µm thick thermal oxide layer. In order to get a flat backside surface, we first use chemical mechanical planarization (CMP) to polish the backside of wafer. Next, the front side oxide is etched in BOE for approximately 10 minutes until the frontside of the wafer becomes hydrophobic. Afterwards, etching the wafers and they are cleaned in the Cintillio to remove all the organic and metallic contaminations. After the wafers are cleaned, a layer of thermal oxide with thickness 1 µm is grown on both sides of wafer. Another 2µm of PECVD oxide is also grown to thick backside oxide. The oxide layer on the backside is used to act as a hard-etch mask during deep reactive ion etching (DRIE).

4.2.2 Patterning of the backside oxide layers

Before the resist is spin coated on the backside of wafer, the wafer is primed with TriMethylSilylDeEthyAmine (TMSDEA) to provide a well defined contact angle of the oxide surface before resist is applied. HPR504 photo-resist is spin coated to a thickness of 2.8µm. To pattern the micro-channels structure in the resist, the micro channel mask is exposed using a contact aligner with an UV intensity of 6.5 mW/cm^2 for 20 seconds with hard contact lithography. Since the positive photo resist (HPR 504) becomes soluble after exposure, we use developer on the ACS track to develop unwanted resist. During this step, some developer may flow and contaminate the front side of wafer. To remove the developer residues from the front side of the wafer, the wafers are rinsed in DI water after development. Then, 3µm thick oxide layer on the backside is etched in the Applied Material Precision 5000 etcher. In order to finish the pattern on the backside, the final step is to strip the remaining resist. This is done by a descum in the oxygen plasma IPC Barrel followed by stripping in acetone twice.

4.2.3 Fabrication of the heater structures on the frontside

For the fabrication of the resistive heaters an aluminum layer with thickness 0.7µm is sputtered first. Next a layer of HPR504 resist is spin-coated to a thickness of 1.37µm. Using hard contact lithography; the heater pattern is exposed with an exposure time of 7 seconds. To improve the adhesion of the resist for the next wet etch step, the wafers are backed in a convection oven for half an hour at 90°C. Next, we remove the Al layer in PES etch for 7 minutes to make sure Al structure is etched completely. After etching the resist is stripped in acetone. Finally the wafer is cleaned in fuming HNO_3.

Afterwards, the second layer on the front side, a 0.7µm thick Nitride (Si_3N_4), is deposited on top of the Al heaters. Before spinning coat a 1.3µm thickness HPR504 layer, TMSDA is also used to improve the adhesion between the Si_3N_4 layer and

HPR504. After exposed for 10 seconds, the resist is developed. Then the front side of wafer is dry etched. Later, resist is dissolved in barrel entirely.

4.2.4 DRIE etching of the micro-channels

Next, because of the design idea, the micro-channels are etched of 500µm depth from the backside of the wafer. The backside oxide layer serves as a hard-etch mask during the DRIE. The DRIE etch was done in an STS-ASE machine using the Bosch process (SF_6 and C_4F_8 plasma) in an ICP (Inductively Coupled Plasma) reactor.

Figure 4.3 depicts some SEM microphotographs of the micro-channels (9 channels). As can be seen from Fig. 4.3(C), the channel width at the bottom is larger than top. This sidewall slope comes from the dry etching process and depends on several process parameters, such as gas flow, chamber pressure and temperature. To improve the slope problem, these parameters should be tuned and optimized carefully in the future.

(A)

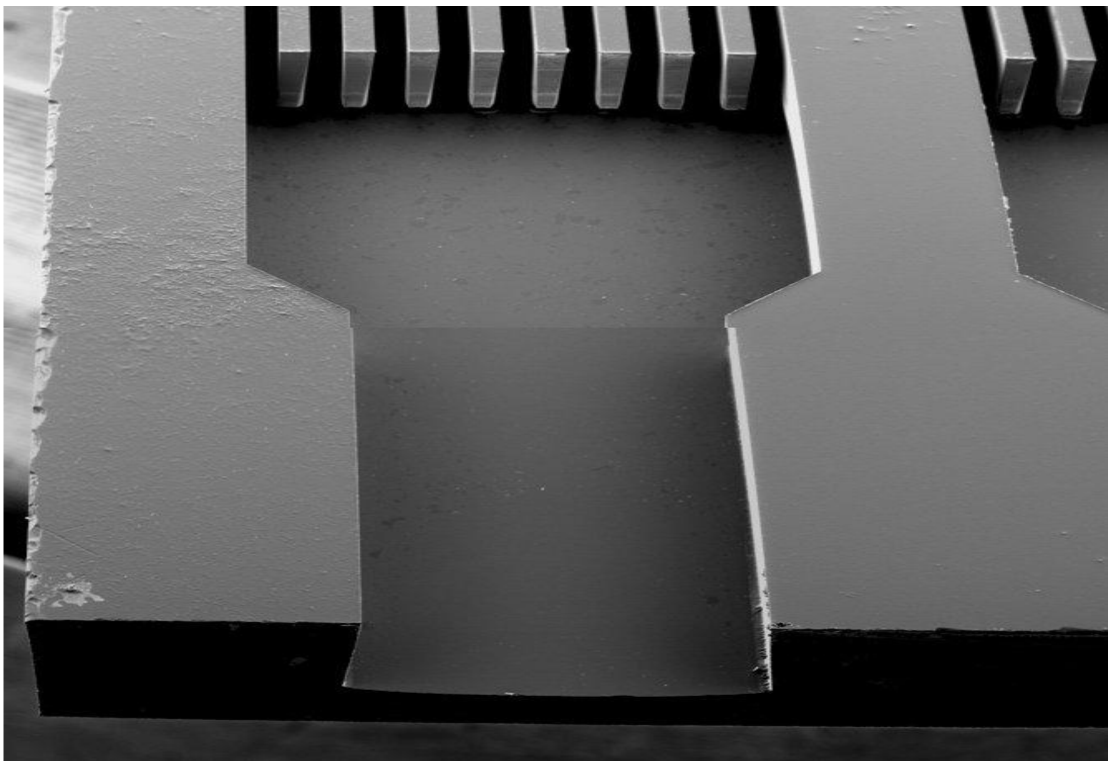

(B)

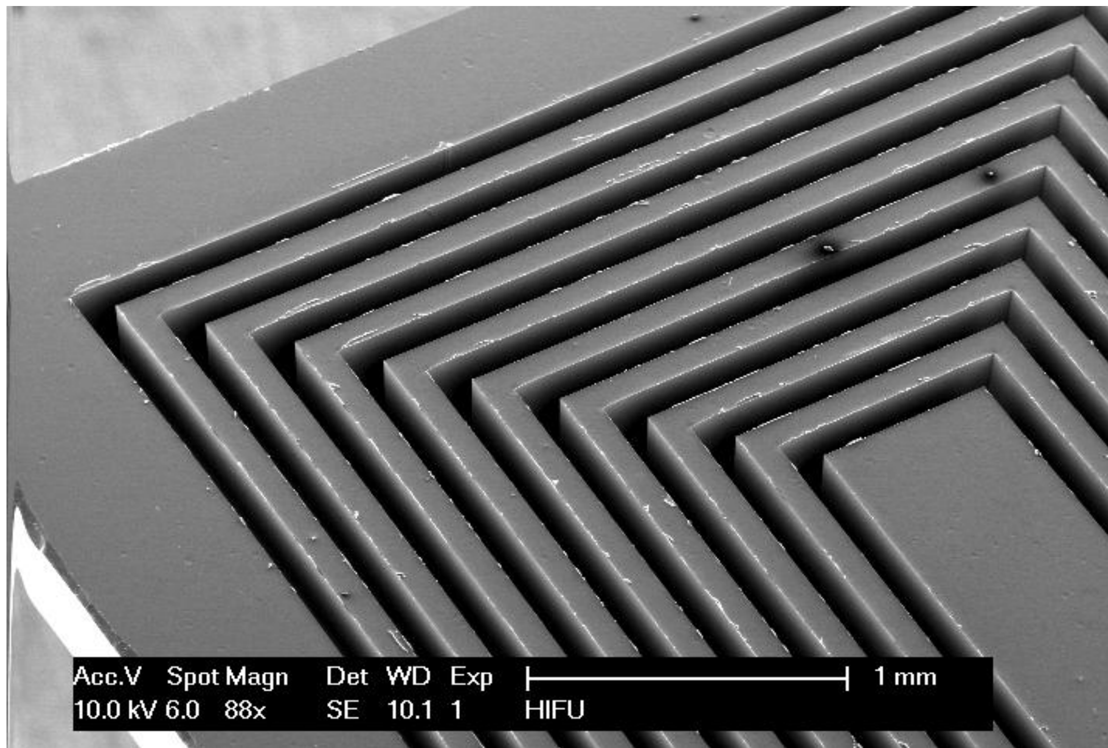

(C)

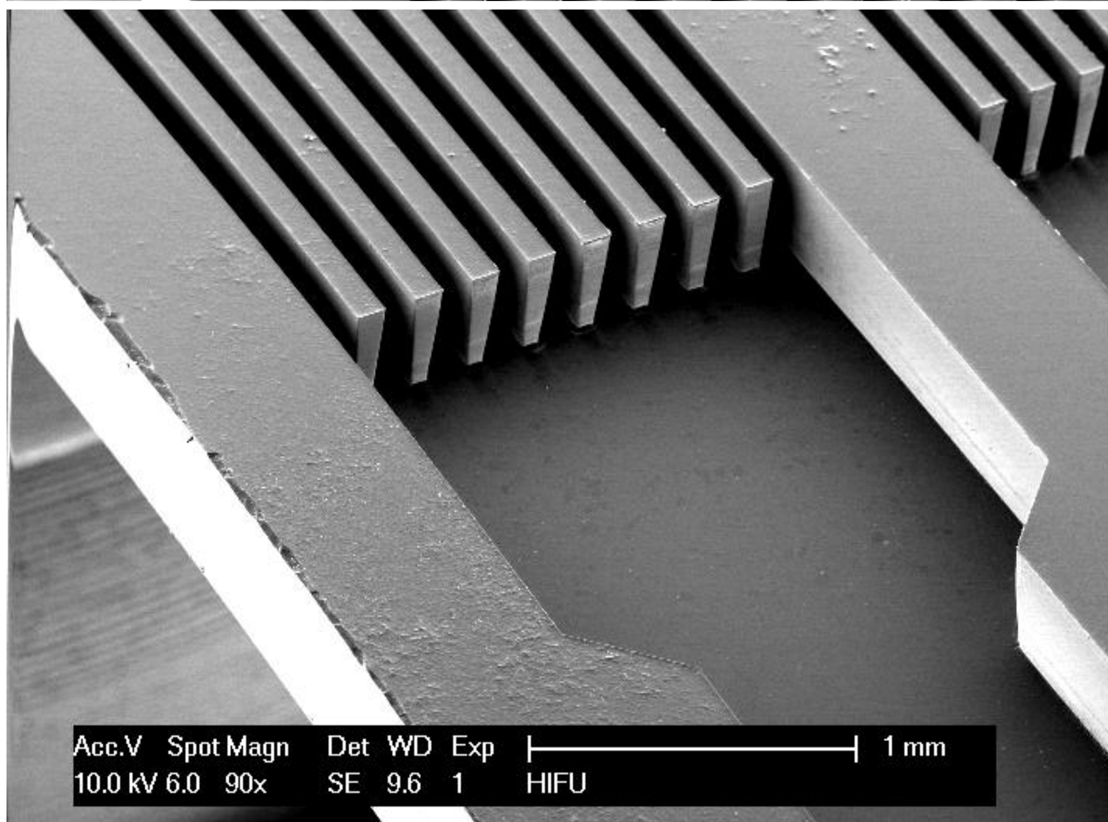

Figure 4.3- SEM micrographs of the micro-channels after DRIE.
(A) (C): The cross section of entrance part
(B): The cross section of U shape part of micro-channel

4.2.5 Discussion

In the design, we expect to have the same 500 μm depth of the channels regardless of the width of the channel. However, there are two main problems during the practical process which make our samples fail to meet this requirement. Firstly, a characteristic of the DRIE etching process is that the etch rate depends of the width of the structures to be etched: the silicon in large structures is etched considerably faster than in small structures. As mentioned in Chapter 3, in order to find a relation between cooling capacity and heat transfer contact surface area, the devices are designed to archive different heat contact surface areas with different numbers of channels. As a result the depth of the channel in the 2-channel device is much deeper than in the 9-channel device. In Fig. 4.4, the difference between the depths of the channels for these devices is around 83 μm which cannot be neglected.

In addition, the 3 μm oxide layer on the backside is not thick enough for the 500μm etching. Before we reach the target of 500 μm depth, all the backside oxide layer is already etched completely due to the limited selectivity towards oxide. Theoretical, to solve this etching problem, there are two methods: (1) Deposit a thicker thermal oxide layer. (2) Deposit a thicker PECVD oxide layer directly. Both methods can enlarge etching time and increase etching depth. However, in our case, since the aluminum structures was already finished before DRIE etching, the better solution is the second method to deposit a thicker PECVD oxide layer on the backside of wafer

(A)

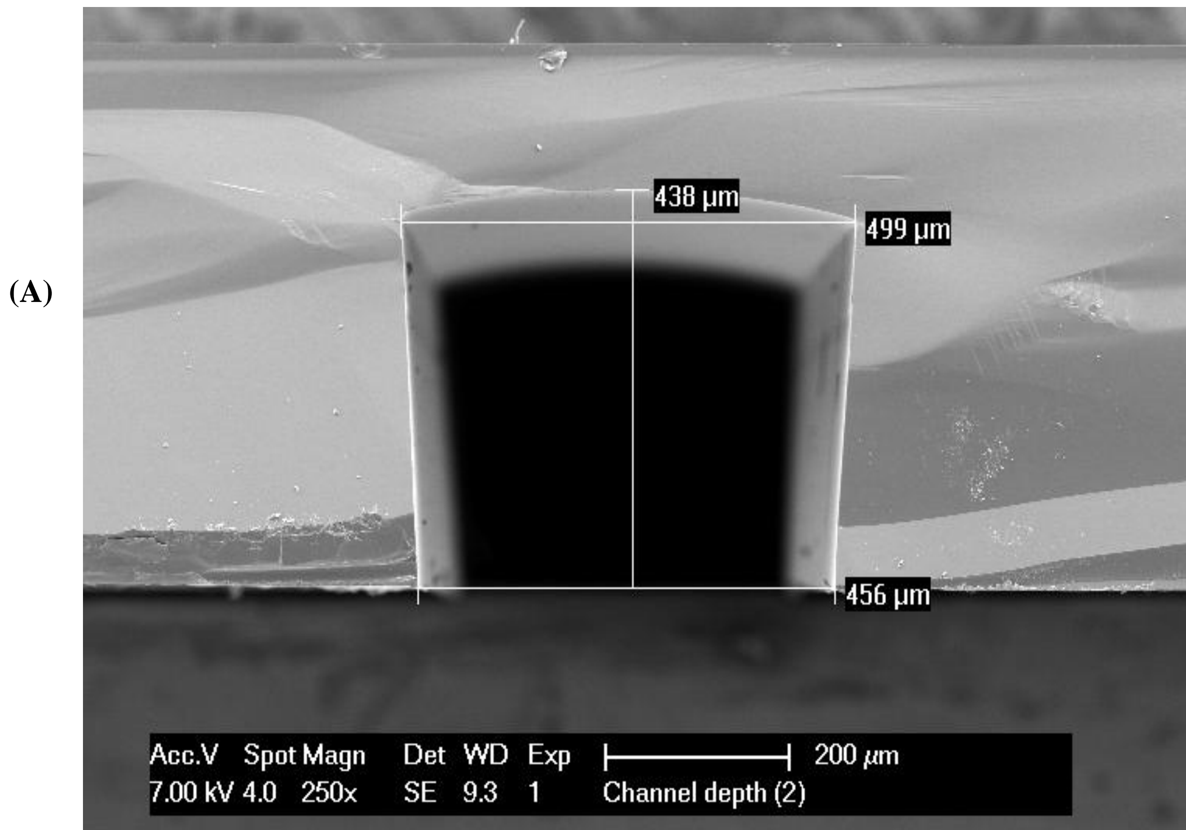

(B)

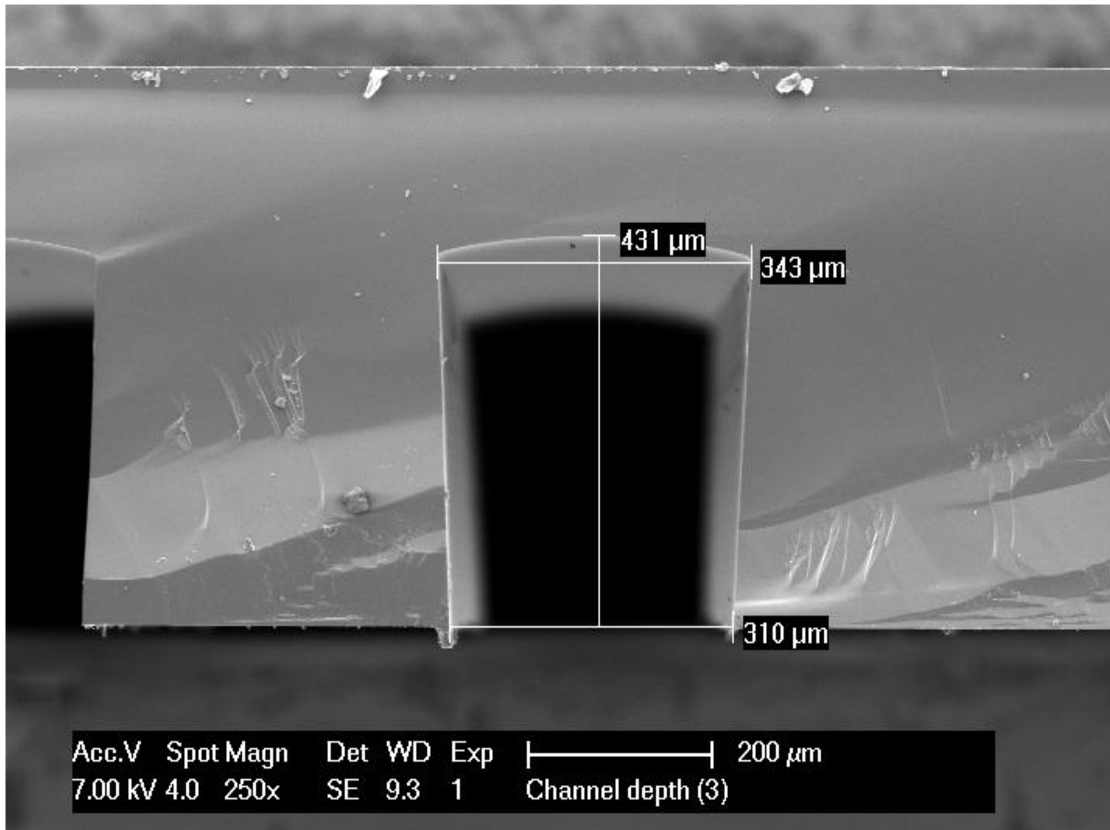

(C)

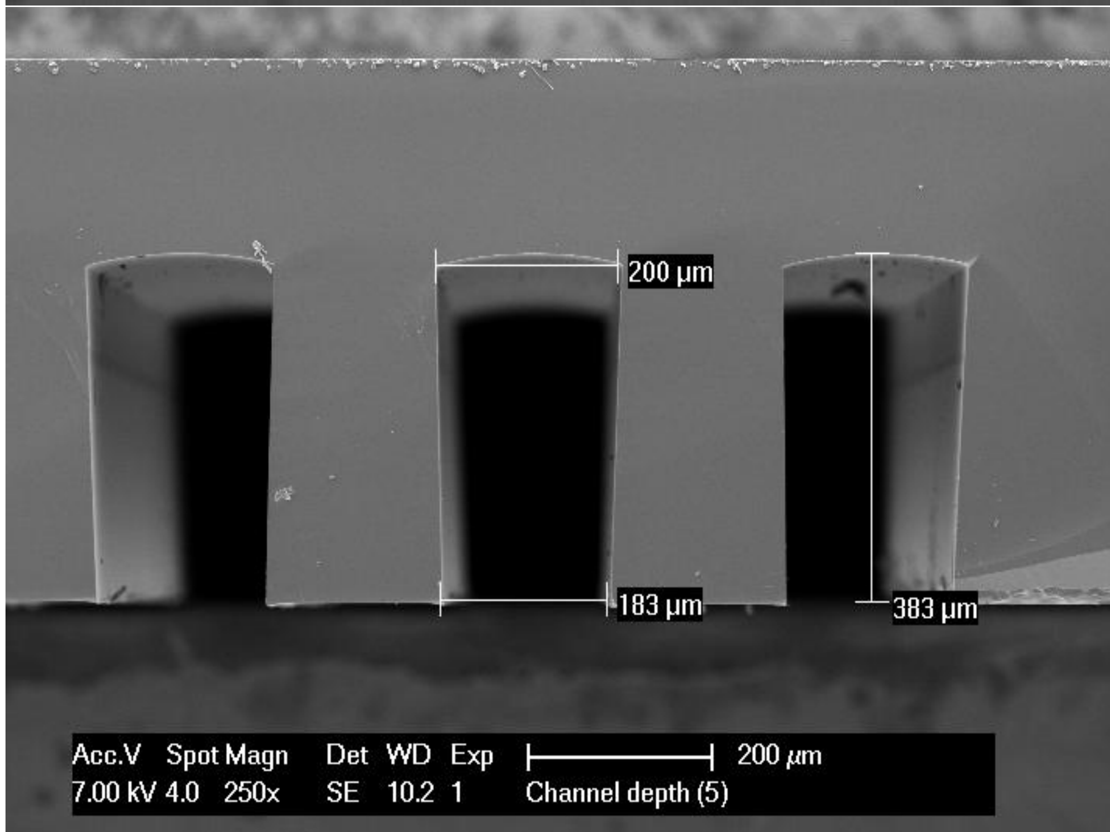

(D)

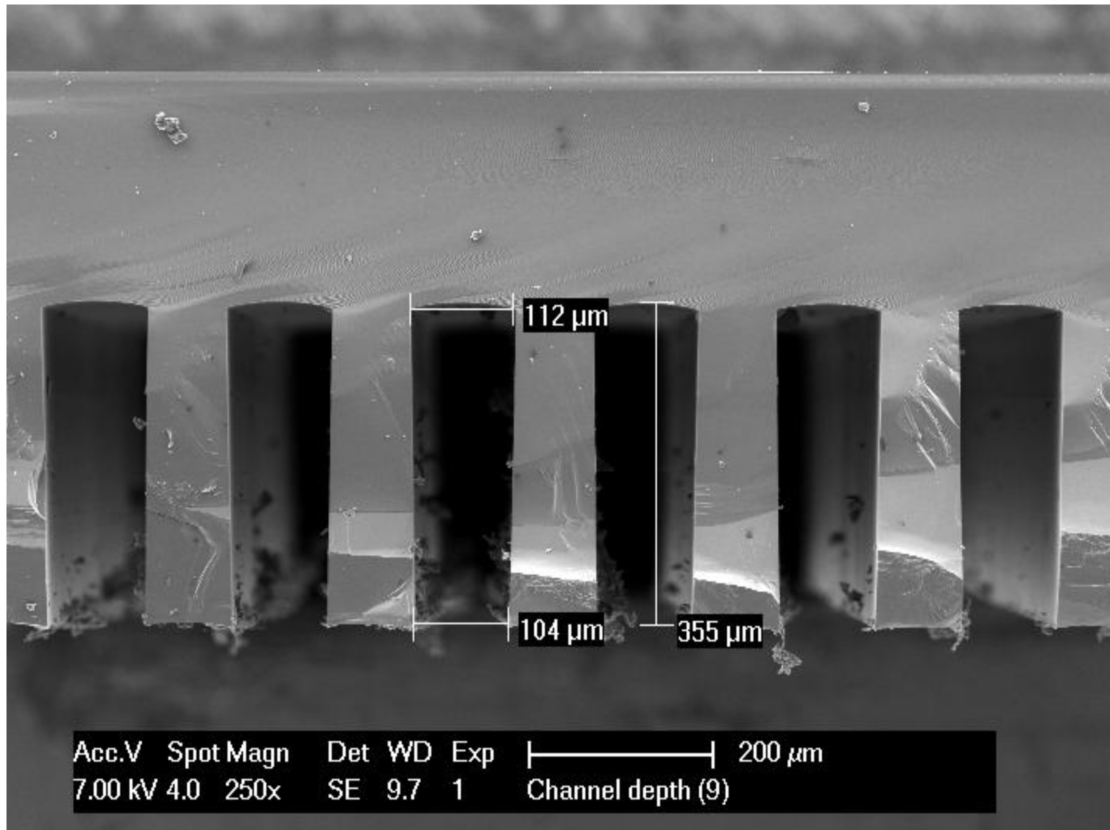

Figure 4.4-The real geometry of cross section with different channels.
(A): 2-channel chip; (B):3-channel chip;
(C): 5-channel chip; (D):9-channel chip

To test the second option in a fast way, a short loop process was carried out. In this short loop, we only focus on the channel structures on the backside of wafer. To simply the process, a 3µm PECVD oxide layer was deposited on the backside of the wafer instead of the 2 µm thick layer one in the previous full process run. Now the 2-channel device could be etched to a depth of approximately 560µm. And the shallowest of 9-channel structure is nearly 450 µm (Fig. 4.5). However, the thicker oxide layer also has a disadvantage. In the short loop, the bow of wafer changes from 0.91 µm (with 1µm thermal oxide) to 22.2 µm (with 1µm thermal oxide and 3 µm PECVD oxide) , which can result in accuracy problem during wafer scale BCB bonding. Additionally the difference in height between the wide channels and the narrow channels increases from 83 um to 109 µm (Fig. 4.5).

(A)

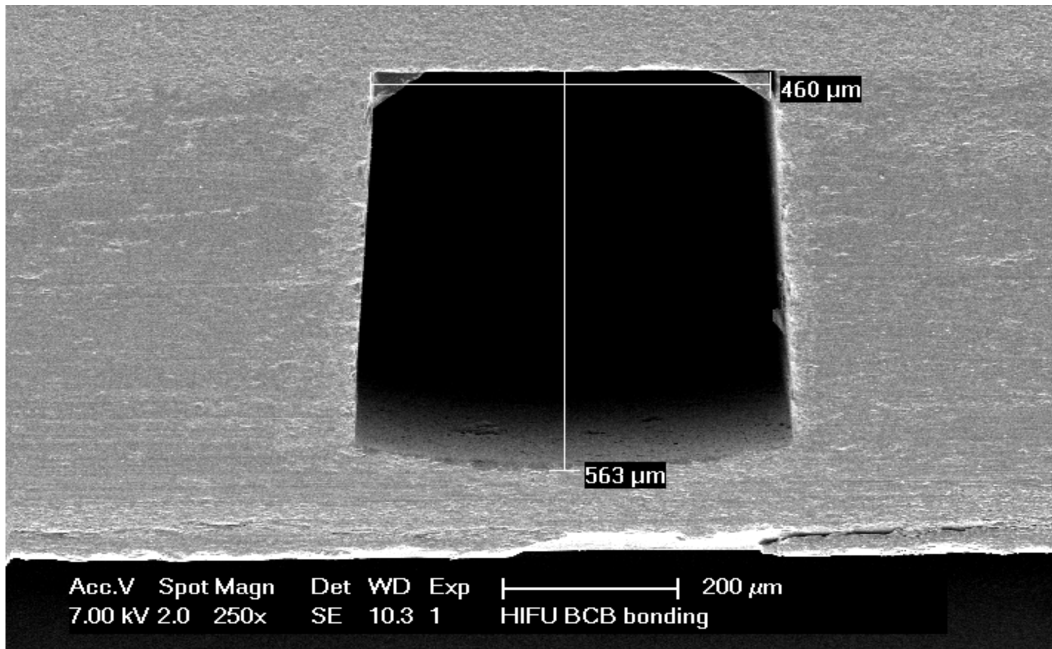

(B)

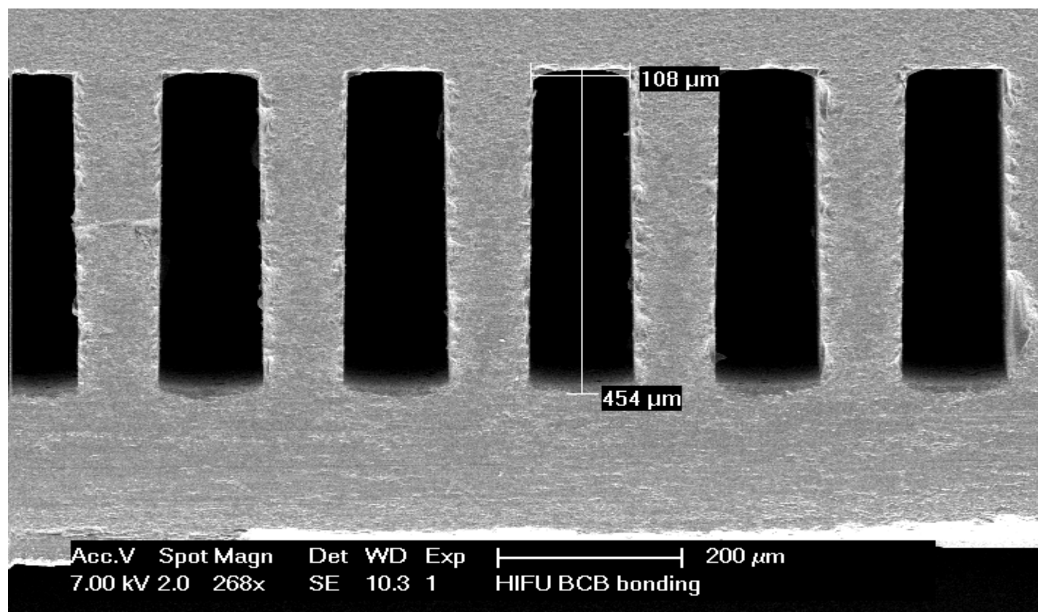

Figure 4.5-(A): Cross Section of 2-channel structure with 563µm depth
(B): Cross Section of 9-channel structure with 454µm depth

- These two SEM pictures are taken after short loop of wafer level bonding, when the silicon wafer is already bonded with glass wafer in the pictures.

4.3 Packaging and interconnections

Due to the medical security requirement, this HIFU device needs hermetic sealing of two strips with same micro-channel design to ensure all the water be contained in the micro-channel. Therefore, after manufacturing wafers in the clean-room, the micro-channels need to be sealed by bonding. This process is very important because

a poor bonding can result in leaky channels and unpredictable results. In this project, we test two packaging methods, chip level bonding and wafer level bonding.

And electrical interconnections in this project are also vital. The electrical wires connecting between chip bond pads and PCB are used to ensure the Al resistive heaters can be electrically connected as well.

4.3.1 Chip level bonding

Using a dicing machine, the silicon wafer is diced into individual chips guided by the dicing markers.

The simplest way to seal the channels is to glue two chips with etched channels back-to-back with an adhesive. To do this, we spread epoxy glue on the clean backside of chip and then stack two chips carefully. UHU Plus Endfest 300 is used for gluing with one-to-one mixed ratio of binder and hardener gel. The gaps between chips are also sealed with UHU Plus. After baking for nearly one hour at a temperature of 80 ℃ to ensure proper adhesion of the different chips, the packaged device is strong enough. Then, in the next step, a syringe tip with a suitable diameter is inserted into the entrance port of the chip and fixed with glue Araldite 2000 plus. The final device is shown in Fig. 4.6.

The manual gluing procedure has the advantage that it is simple, quick, and when properly performed offers a perfect sealing of the channels. The biggest disadvantage is that the adhesive can creep into the channels. Worst case the inlet and outlet are blocked completely. Unfortunately the device is not transparent so any blockage of a channel can remain unnoticed.

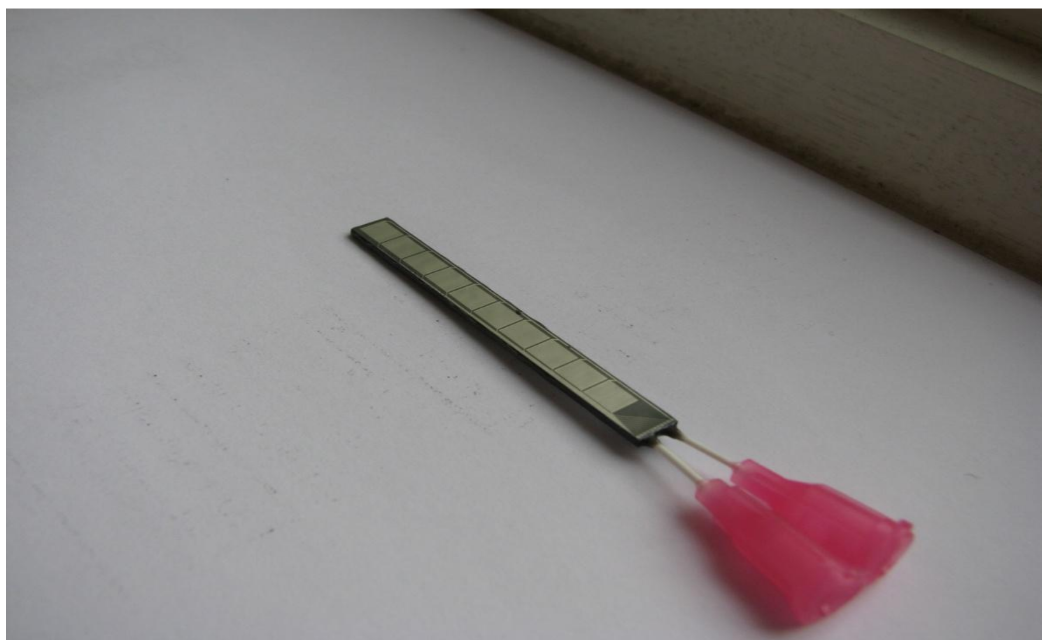

Figure 4.6-The packaged device with chip level bonding

4.3.2 Wafer level bonding

Wafer bonding is the packaging technology on wafer-level suitable for the contacting of at least two wafers with or without an intermediate layer. The most common techniques are: silicon direct bonding, anodic bonding, eutectic bonding, seal glass bonding and adhesive bonding [20]. Compared with other boding methods, the adhesive bonding doesn't require two extremely flat wafers. The pattern wafer, such as our wafer with microchannels is still suitable to adopt this method. And another advantage of adhesive bonding is this method only needs a low bonding temperature, which is no higher 250℃ in this project.

BenzoCycloButene (BCB) is a benzene ring fused to a cyclobutane ring, whose molecular formula is (C_8H_8). The advantage of BCB over other polymers, not only in its low dielectric constant, a low dissipation factor at high frequencies, low moisture absorption, and high degree of planarization, but also in its ability to form high aspect-ratio micro-structures [21-22].

Wafer bonding with adhesive glue (BCB) is a process based on polymerization reaction of organic macromolecules. During polymerization, the organic molecules (monomers) will form long polymer chains. The energy for the polymerization reaction comes from the annealing process. After the cross-link reaction, the BCB becomes a solid layer of polymer, which forms the basis of adhesive bonding.

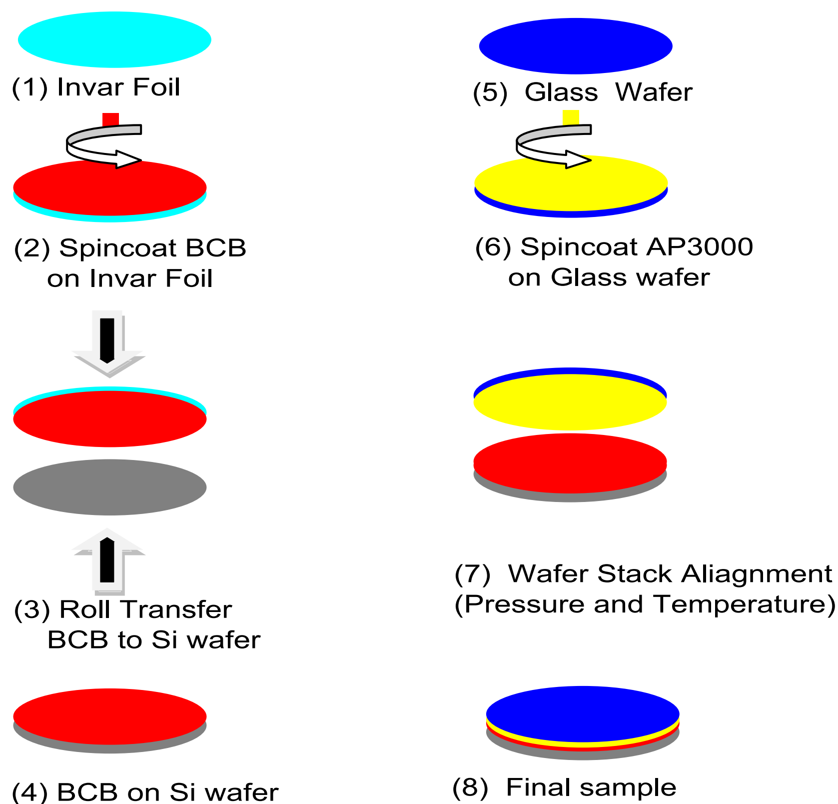

Figure 4.7- The schematic of Si-Glass BCB bonding process.

The complete wafer level BCB bonding process in our project (two Silicon wafer bonding) could not be fully carried out due to the limited time available. However, the most important steps of the process were tested by Si to glass bonding. The silicon wafer used in this experiment is taken from the short loop from improving DRIE etching, which had a similar micro-channel structure as the wafers used in the full process run. The silicon wafer was glued to a glass substrate so that the bond quality could easily be inspected.

The full process (Fig. 4.7) consisted of: (1) BCB roller transfer to the silicon wafer. (2) Bonding of the silicon wafer to the glass wafer. The detailed process can be found in Appendix B.

(I) BCB roller transfer

The BCB bonding process starts with the cleaning of an invar foil with a short descum in the Barrel IPC 9200. This invar foil is a kind of flexible stainless foil, which is easy to bend and mount on the roller for transferring the BCB to the silicon wafer. Then the invar foil is spin coated with 5ml BCB (CYCLOTENE 3022-46). CYCLOTENE 3022-46 is an advanced BCB polymer with an anti-oxidation additive dissolved in mesitylene. After spin coating, the BCB mesitylene solvent is evaporated from the BCB layer by baking on a hot plate at 95℃ for 3 minutes. Proper evaporation of the solvent is important to obtain a bubble free adhesive layer. While the BCB layer on the invar foil is being baked in the hotplate, the silicon wafer is prepared for gluing with an oxygen descum in the barrel to clean and remove all the contaminations on the surface. Next, the invar foil is mounted on roller and the silicon wafer is placed on the hotplate at 100 ℃, which is in front of the roller. And as shown in Fig. 4.8, the BCB layer can be transferred from the invar foil to the Si wafer by moving the roller with the invar foil over the silicon wafer (velocity: 3mm/sec). However, after this step, the BCB layer on the silicon wafer is still roughness. In order to get a smooth BCB layer, the wafer is baked on hot plate at 150 ℃ for 15 minutes. Under that temperature, the BCB reflows to become a smooth layer.

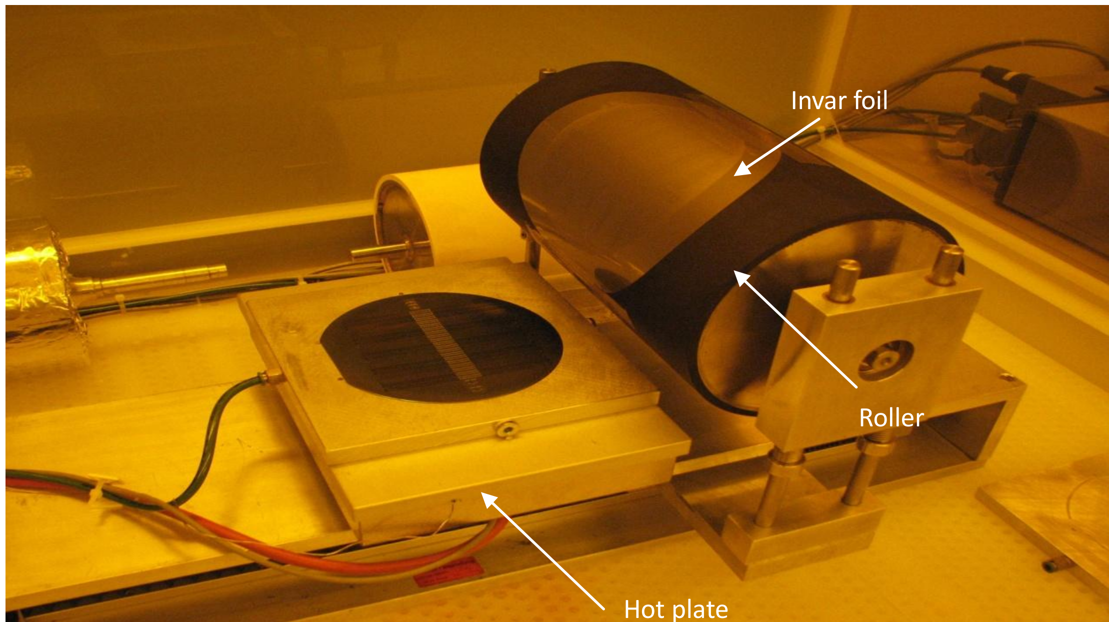

Figure 4.8- The transfer of the BCB layer to the silicon wafer using the roller.

(II) Bonding of the silicon wafer to the glass Wafer

Next, the glass wafer is prepared for gluing. After descumming in oxygen plasma at the Barrel, 5ml adhesion promoter (AP3000) is spin coated on the glass to increase the adhesion between a BCB layer and glass. The glass wafer is bonded to the silicon wafer using an SÜSS MicroTec wafer bonder. Figure 4.9 shows the silicon and the glass wafer fixed on the wafer rig ready for gluing. Wedge shaped spacers of 100 um thickness are inserted at the edge of the wafer stack. Then a graphite and Al foil is covered on the glass wafer. The graphite is used to keep pressure uniformly over the whole wafer surface area and the aluminum foil is used to avoid the stickiness phenomena between the bonder machine with top of wafer. Bonding of the wafers is carried out in vacuum at a temperature of 250°C (Fig. 4.10).

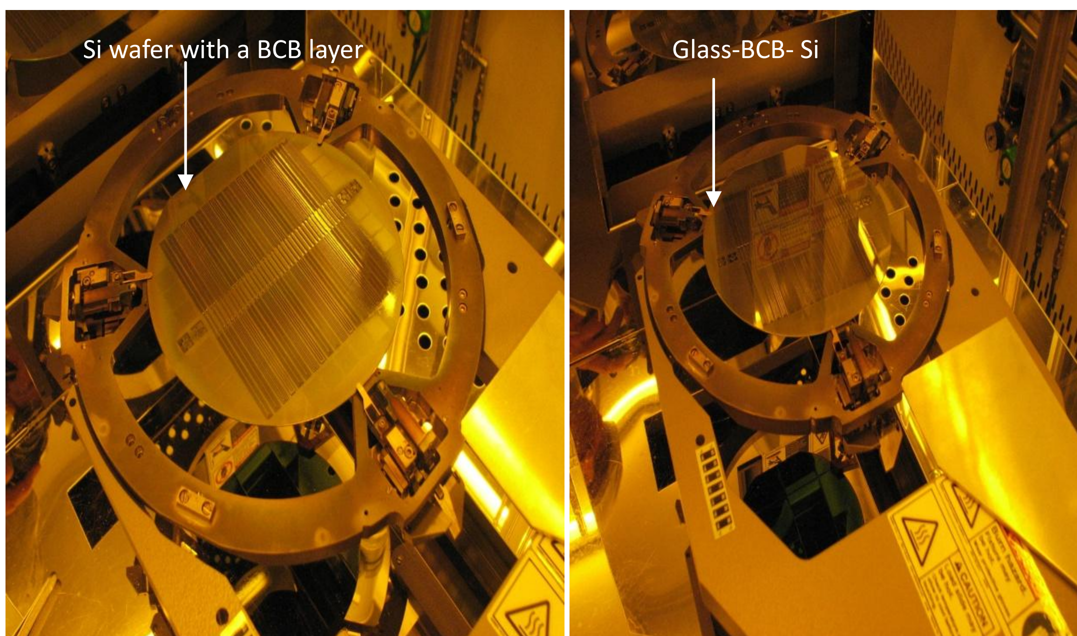

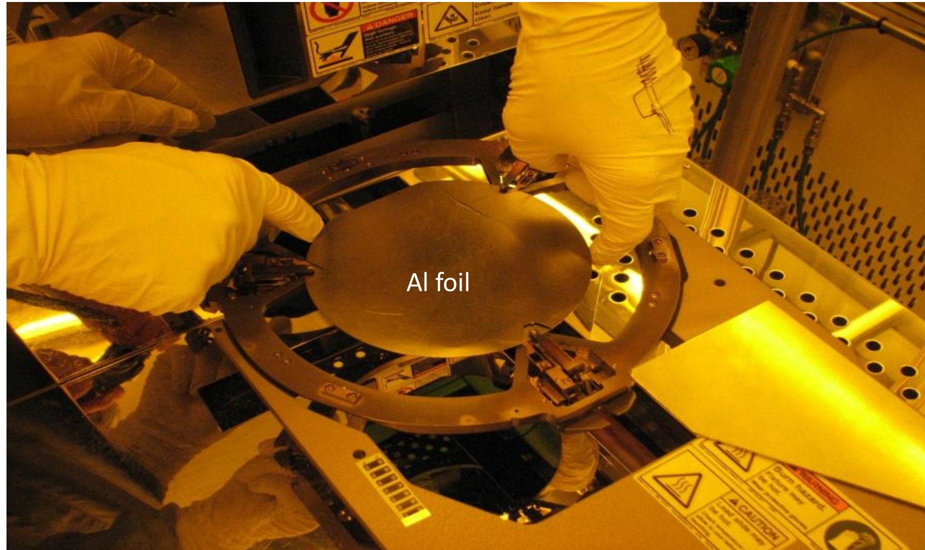

Figure 4.9-Wafer-stack alignment.
(A): Only silicon wafer on the chuck; (B): Glass wafer stacked on the silicon wafer;
(C): Al foil covered on the glass wafer to avoid stickiness

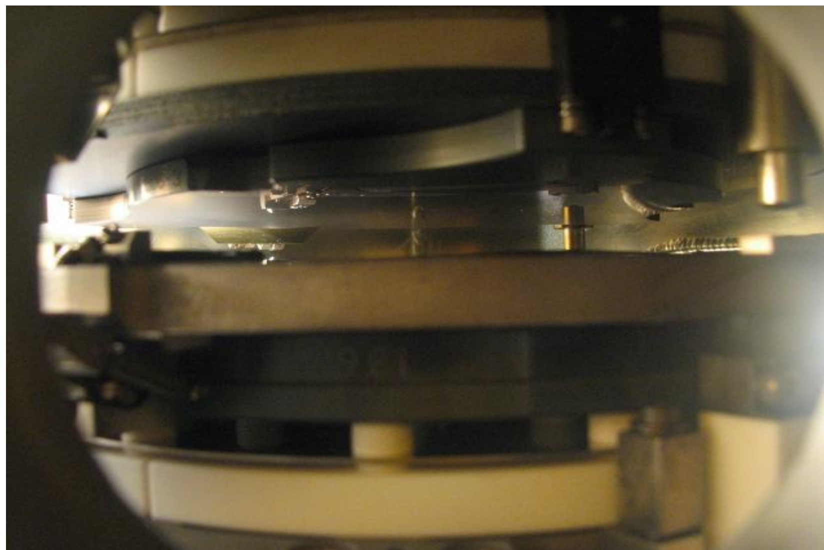

Figure 4.10- Wafer bonding in the SÜSS MicroTec with graphite and Al foil

Figure 4.11 shows an optical microscope image of channels after wafer bonding looking through the glass. It can be observed that at some places the BCB has flown into the channels (colourful and gray parts in the picture).This may block the narrow channels. However, from the SEM cross sections (Fig. 4.12-4.13), it is becomes clear that the BCB only appears at the upper corner of channel, near the interface between the silicon and the glass. And even compared to the narrowest width of channel (≈100μm), the BCB can still be neglected without affecting the normal function of channel

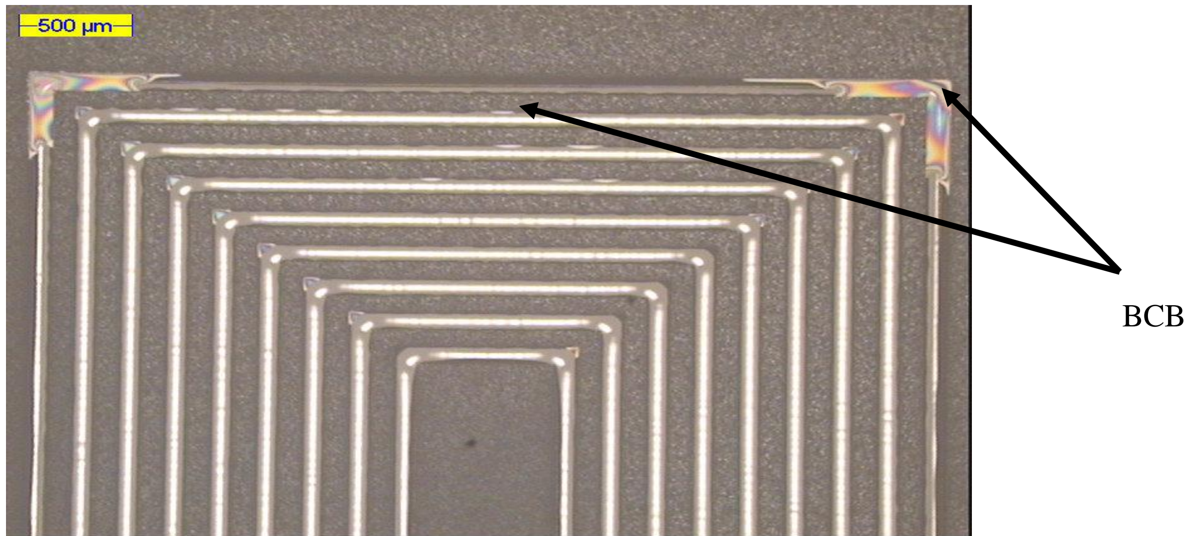

Figure 4.11-Optical microscope image of 9-channel after BCB bonding

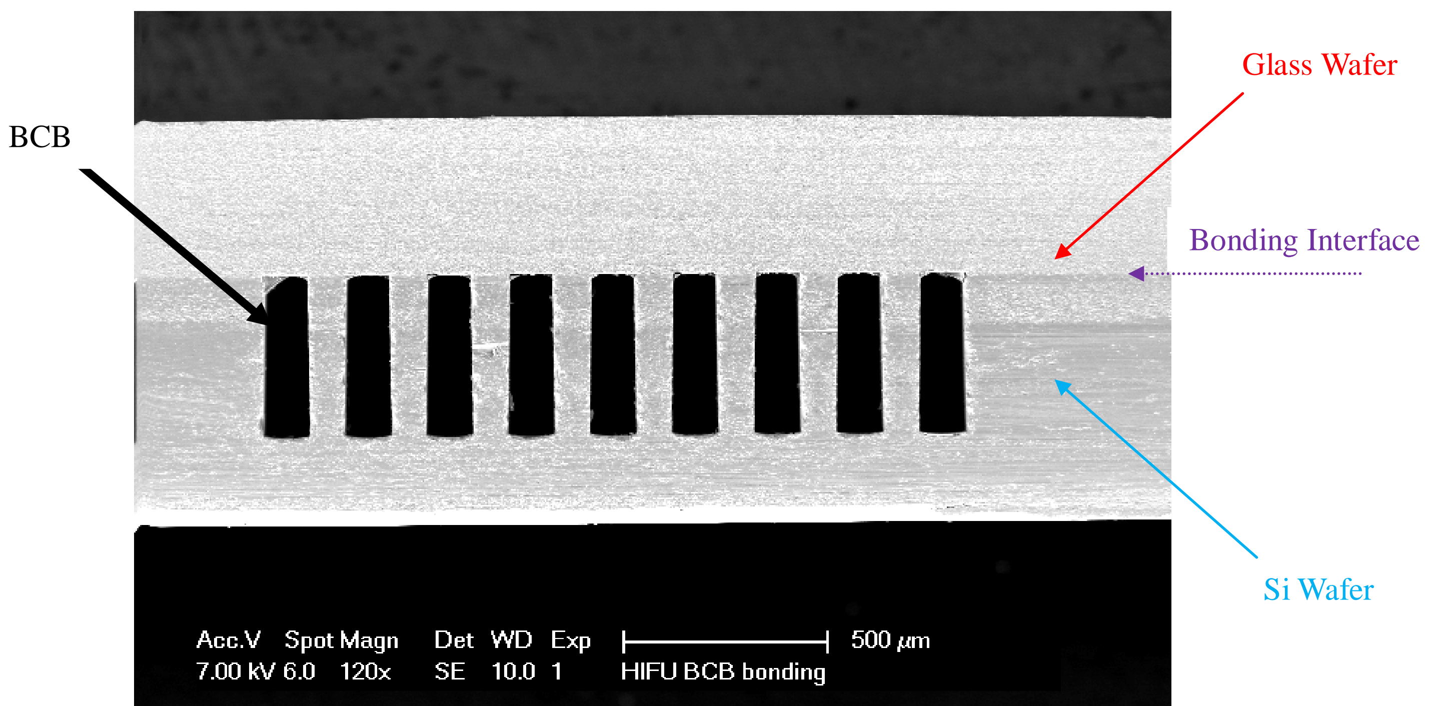

Figure 4.12- Cross Section of the 9-channel part after wafer level BCB bonding.

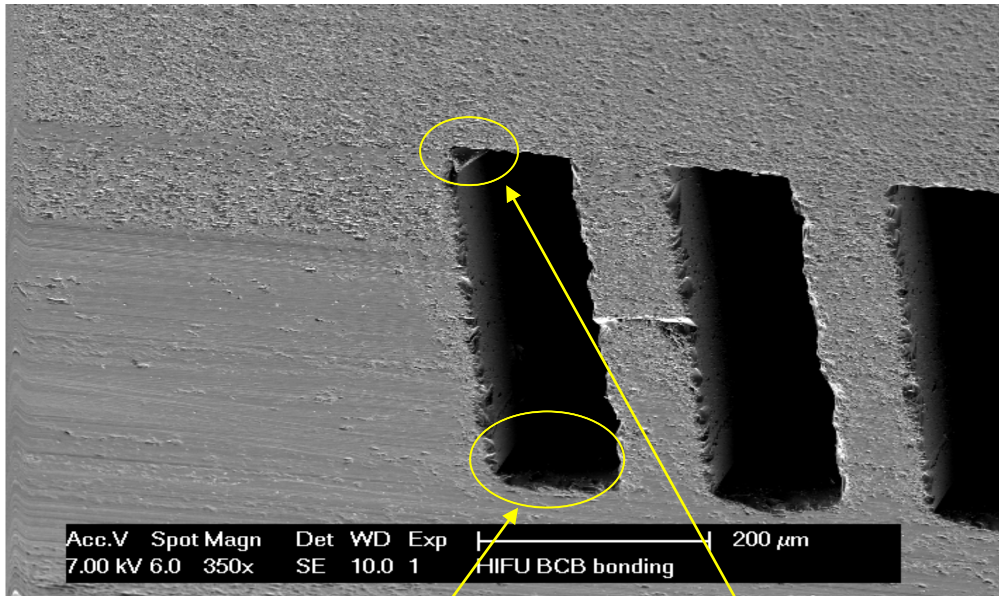

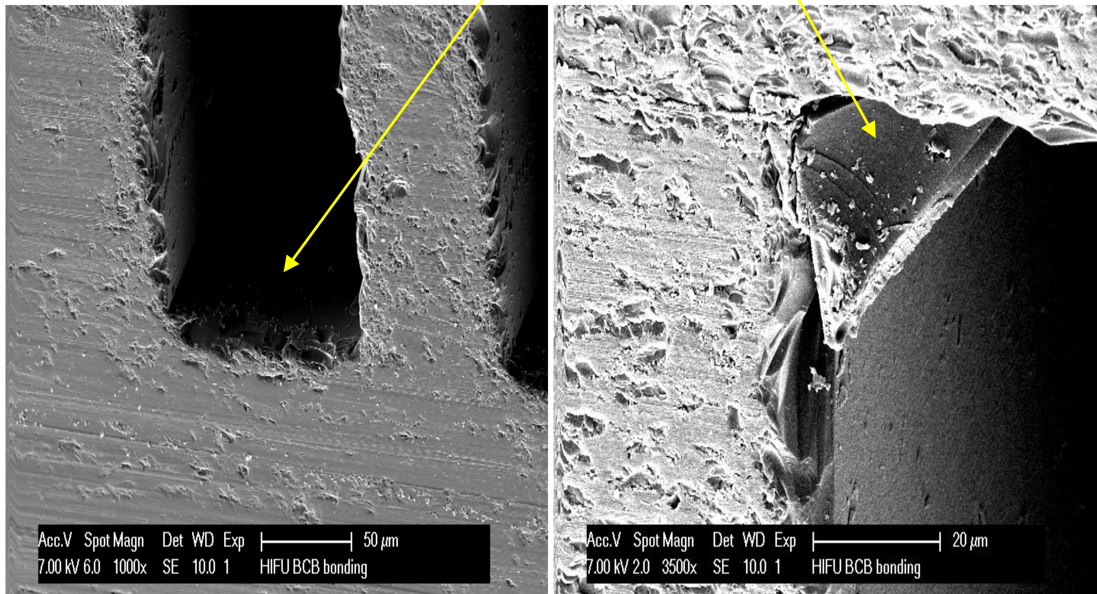

Figure 4.13- Cross Section of 9 channel after BCB bonding observed from different angles.

4.3.3 The electrical interconnections

Two types of devices were fabricated. The first type was designed for testing puposes. It had the electrical connections on one end of the device, and the fluidic connections on the other end. In this way the device could be mounted on a Printed Circuit Board (PCB) which was available from another project in such a way that the electrical wire-bonds were not in the way of the fluidic tubes and visa versa (Fig. 4.14A). The second device was designed exactly as the real ablation device, so with the electrical and fluidic connections on the same side. An assembly specialist at Philips Research mounted this device on the tip of a catheter like instument in such a way that both the electrical as well as the fluidic connections could be accessed (Fig. 4.14B).

(A)

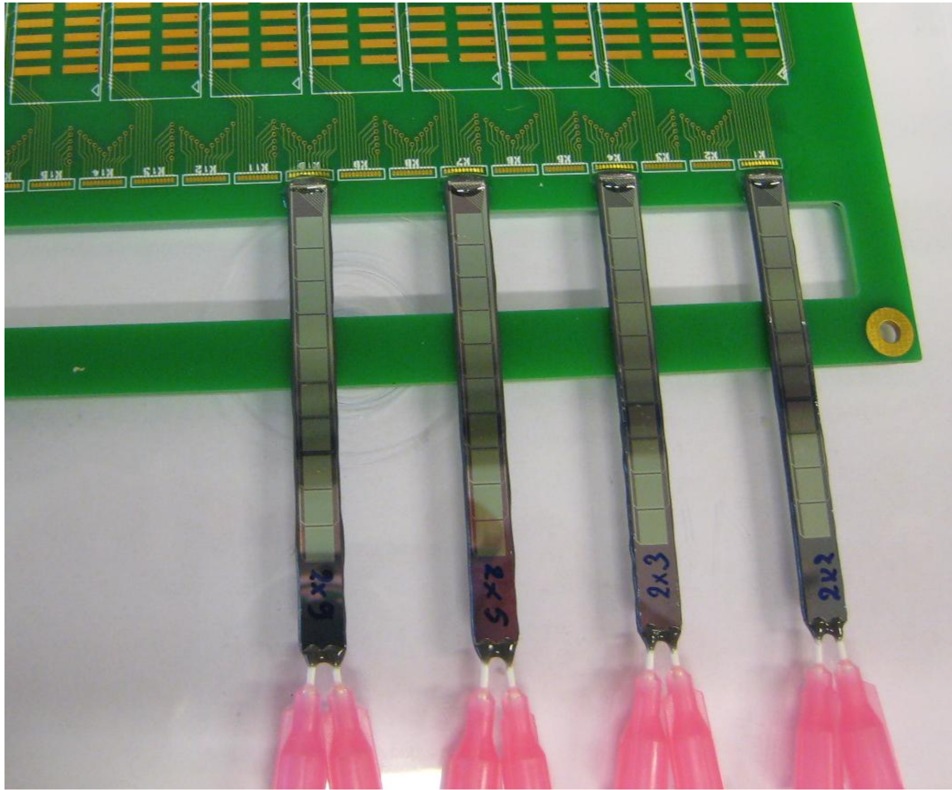

(B)

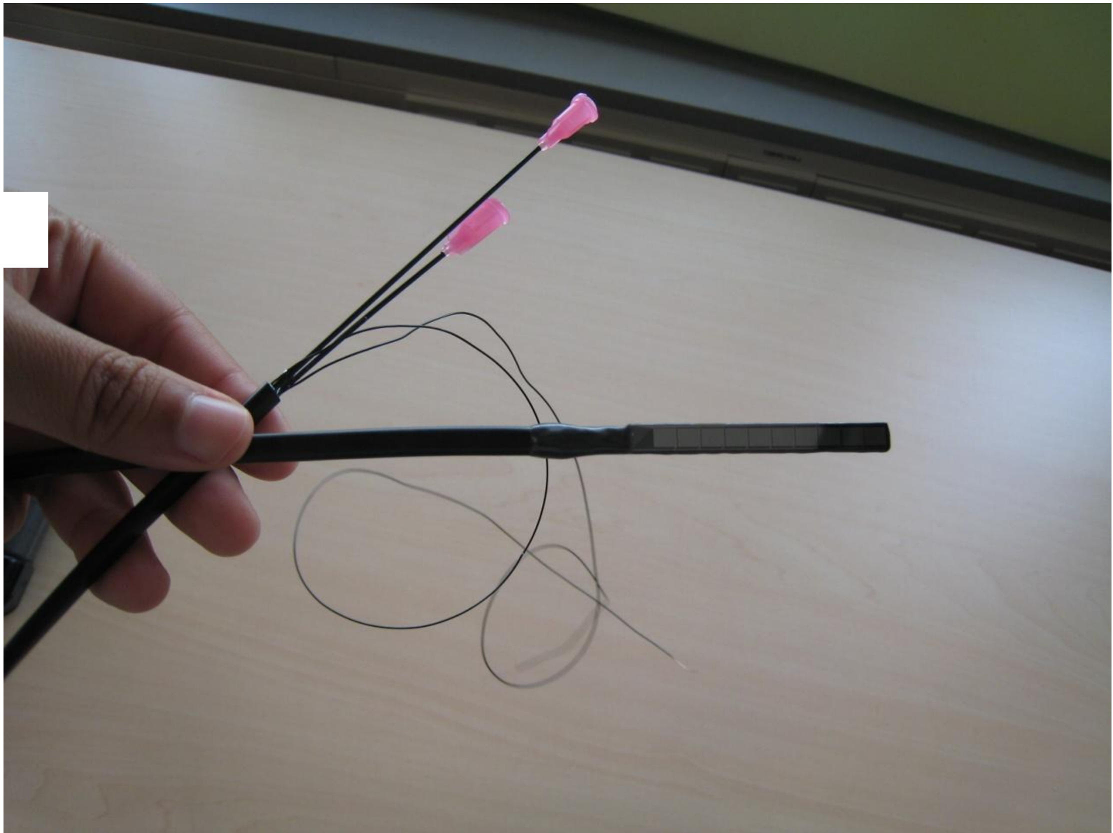

(C)

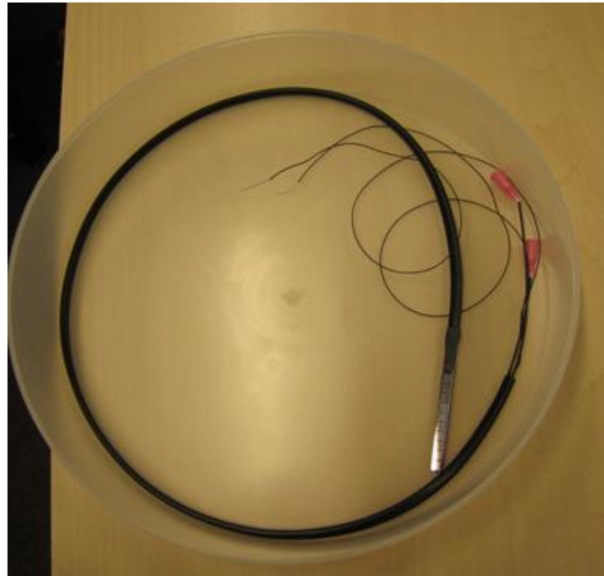

Figure 4.14- Electrical interconnection. (A): test cooling device; (B) & (C): real cooling device.

Chapter 5 Experimental setup and results

5.1 Cooling capacity experiment

5.1.1 Experimental setup

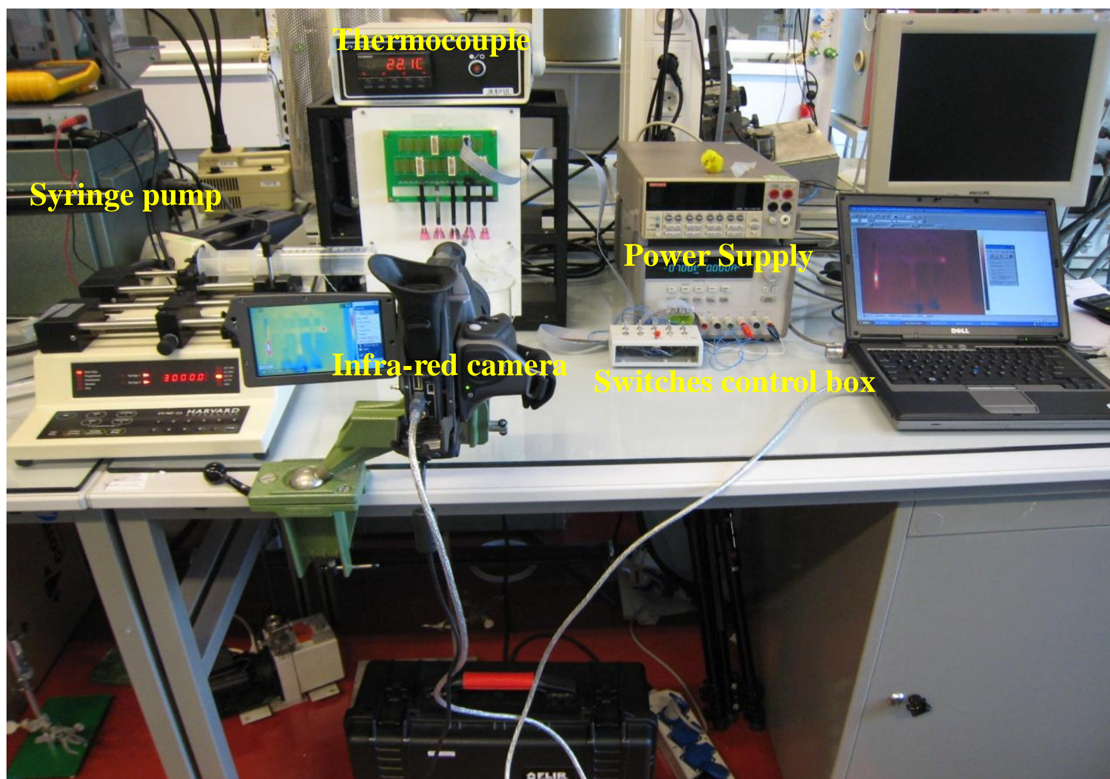

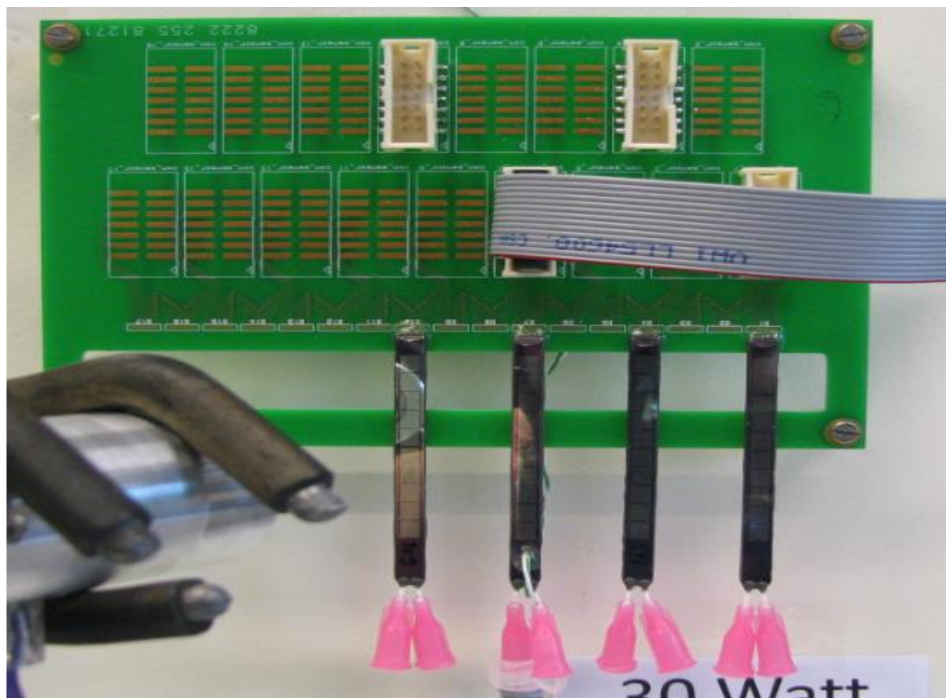

Figure 5.1- The experimental setup for water cooling capacity test

The complete experimental setup (Fig. 5.1) consists of an electrical circuit with power supply (Fig 5.2), a syringe pump Harvard M33, a thermocouple to measure temperature in the lab and an infra-red camera SC660. For these measurements the test devices are used which have the electrical and fluidic connections on opposite sides. The side of the devices with the electrical contacts is glued to the edge of a printed circuit board which provides the interface between the bond pads on the test device and a macroscopic connector. The printed circuit board is connected to a test box with ten switches so that each individual heater can be switched on or off (Fig. 5.2). The syringe pump enables applying inlet fluid flow rate to the cooling device. The PCB is placed in front of an infra-red camera, so that the camera can measure and record the device surface temperature. All the experiments have been done with demi water.

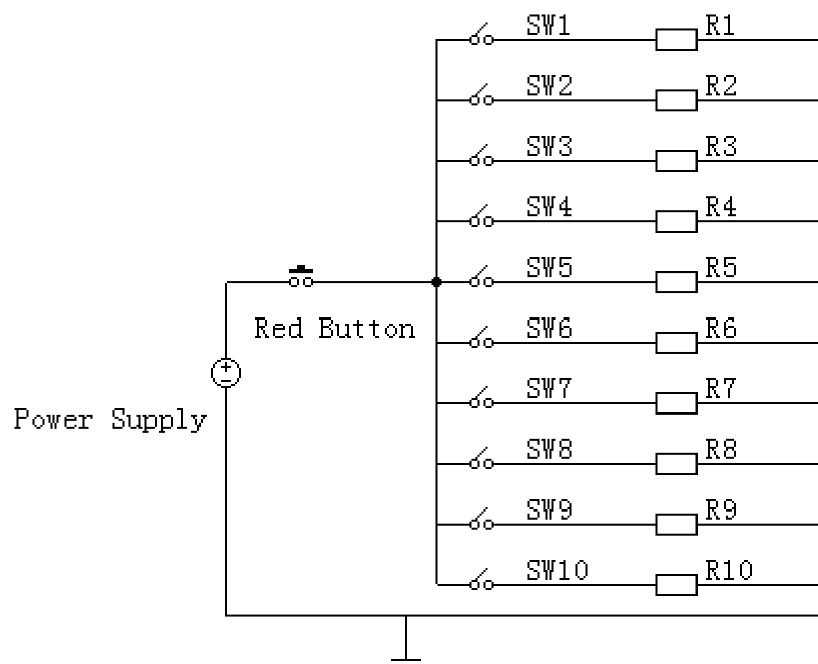

Figure 5.2- The circuit diagram in the cooling experiments

Before starting cooling testing, the flow condition of each test device should be checked first. In the initial set of four samples, the 9-channel device is completely blocked and useless. It is because the width of one micro-channel in 9-channel chip is smallest which is more likely to be blocked. Therefore, a new 9-channel chip is glued and mounted on the same PCB.

The maximum syringe size in the manual of syringe pump Harvard M33 is only 50mL. For saving refilling time, a much bigger syringe of 140mL was used. This change required a calibration for the flow rate of the syringe pump. In the calibration, the pump was set to different flowrates ($Q_{entered}$), and the real volume of outflow water in one minute was measured. The measurements show that there is a linear relation between measured ($Q_{measured}$) and entered flow rates ($Q_{entered}$):

$$Q_{measured} = 0.72 * Q_{entered}$$

5.1.2 Experimental result

In order to explore cooling capacity of test cooling device, several measurements with various power dissipations and with different flow rates have been carried out. To compare the measurements with the FEM simulation results, the 5 channel cooling device was used as the first test sample.

The power dissipation of device is calculated from the applied voltage and the measured current, with an error of +/- 0.1W. The performance of the cooling capacity is determined from the maximum surface temperature of the device (T_{max}), which is recorded by the infra-red camera which has a < 30 mK sensitivity, with an accuracy of +/- 1%. The temperature measured by the infrared camera depends on the effective emissivity of the surface. To reduce the inaccuracy from the reflection of polished surface, the surface of device is painted black so that an emissivity ε=1 could be assumed.

To avoid overheating of the heaters on the test devices in the experiments, the syringe pump was always switched on before the voltage was applied to the chip, Figure 5.3 shows that a small air bubble in the cooling water can cause a quick raise in temperature. The cooling system should therefore always be carefully checked for air bubbles prior to a measurement. Figure 5.4-(A) shows the graph of the recorded maximum surface temperature versus time. After increasing to a peak in a short time, the temperature dramatically decreases for approximately 15 seconds. This phenomenon occurred since that the heaters were switched on too early and the flow had time to stabilize. To improve it, the recording step of temperature should wait for several seconds until observing a stable flow from the outlet of device (Fig. 5.4-(B)).

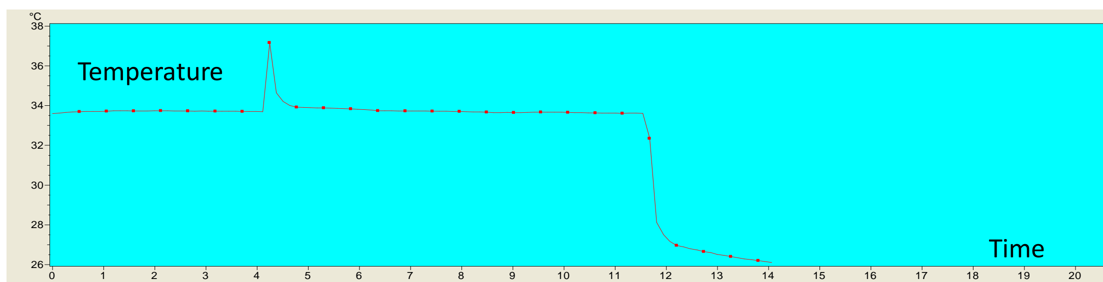

Figure 5.3- Recorded maximum surface temperature affected by air bulb

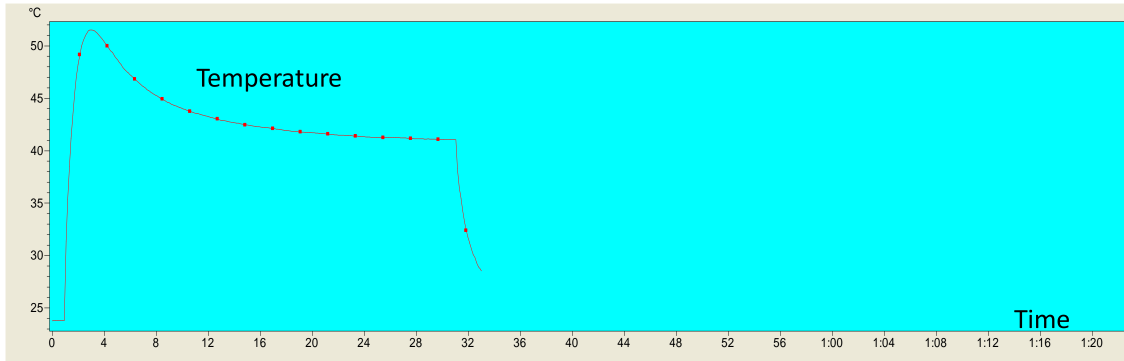

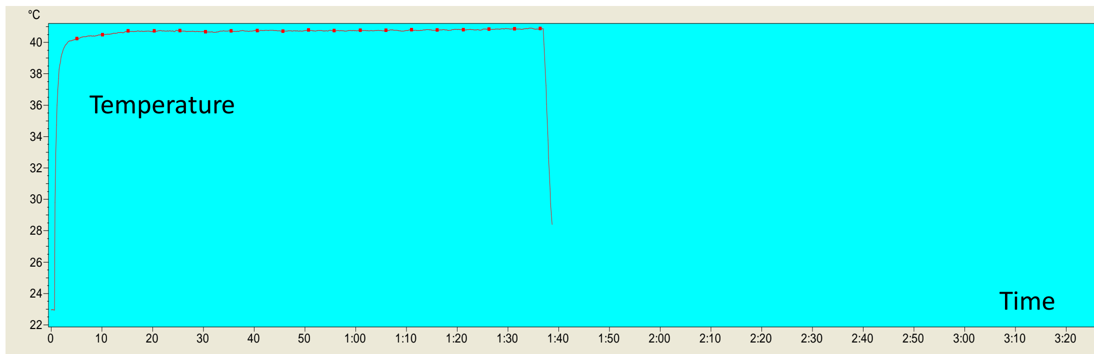

Figure 5.4-(A): The recorded max temperature on the 5-channel cooling device for a dissipated power of 20W, flow rate of 1440mL/hr, which starts before a stable flow is obtained;

(B): The recorded max temperature on the 5-channel cooling device for a dissipated power of 20W, flow rate of 1440mL/hr after the flow has stabilized.

For a dissipation power of 20W in the 5-channel chip, the maximum surface temperature as a function of flow rate is shown in Fig. 5.5. For a flow rate of 1440 mL/hr, the maximum surface temperature as a function of dissipation power is presented in Fig. 5.6. Compared to the FEM simulation data, the measured T_{max} is higher than in the FEM simulations. In other words, the cooling capacity is worse than we expected from FEM simulation.

In the Fig. 5.5, compared to the FEM simulation result, the measured relation has a similar curve. The difference (ΔT) can be explained by several reasons. Firstly, the inlet fluid temperature for simulation is fixed to 20°C, but during the measurement, the water temperature in the lab is around 22°C. After increasing the simulated inlet water temperature to 22°C, the simulation results are shown in Fig 5.7, which proves this explanation. In addition, the height of micro-channels in the test cooling device ($383\mu m$) is much smaller than the ideal design height ($500\,\mu m$) which means the contact surface area of sample is also smaller than the design. Although we also tried to simulate a new model with a smaller channel height, the convergence problem makes this unavailable now. Moreover, the heat flux is uniform in each heater area for the simulations. However, in cooling capacity test, as shown in Fig. 5.8, after fabrication process, there were several heaters (No. 4, 5 and 7) that were defective and

therefore resulting in a non uniform heat flux. All of these reasons lead to worse cooling capacity and a higher T_{max} than expected according to the FEM simulation model.

Notice that in Fig. 5.6, the measured relation is not as same as the FEM simulation. Except the error and accuracy of experiment, the measured result is also affected by radiation and air convection. To simplify the FEM simulation, we enforce a vacuum environment around the device so that all the dissipated power is only transferred only by conduction and convection. In the reality, the vacuum is impossible, which means the influence of convection through air and radiation can't be avoided.

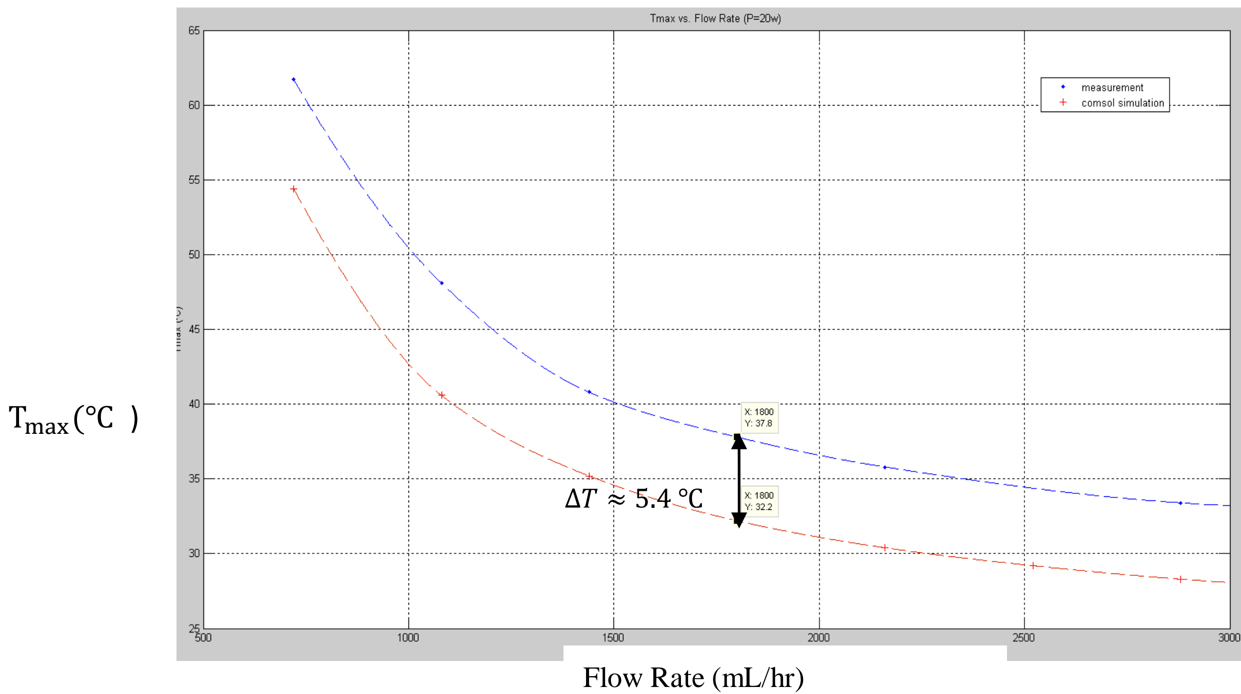

Figure 5.5- The measured maximum surface temperature for the 5-channel cooling device as a function of the flow rate for a dissipated power of 20W compared to FEM simulations.

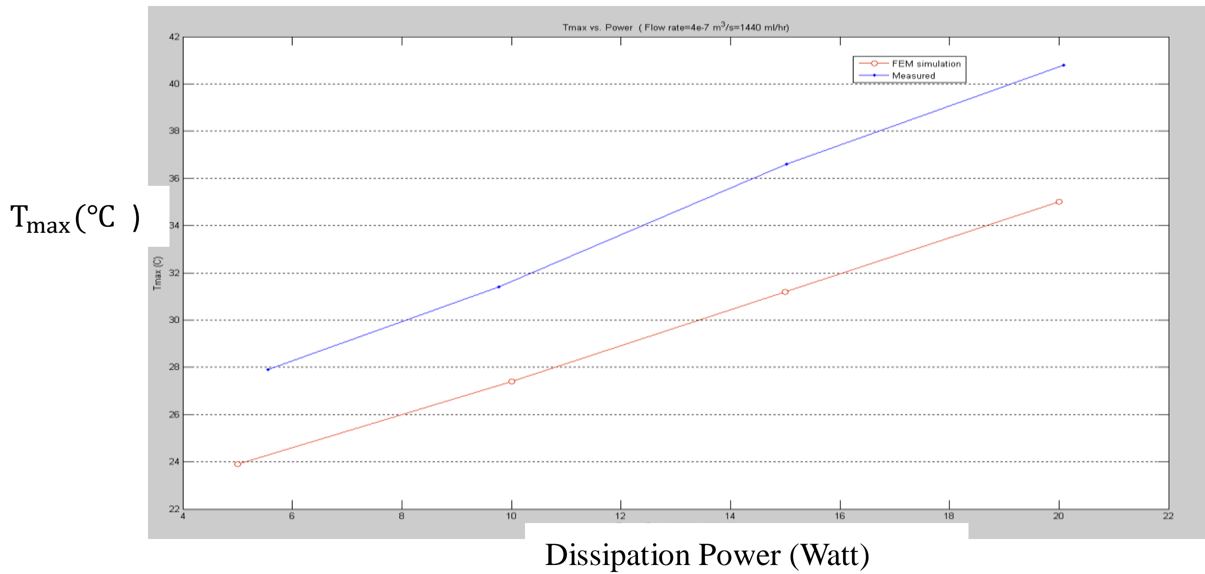

Figure 5.6- The measured maximum surface temperature of the 5-channel cooling device as a function of the dissipated power for a flow rate of 1440mL/hr compared to FEM simulations.

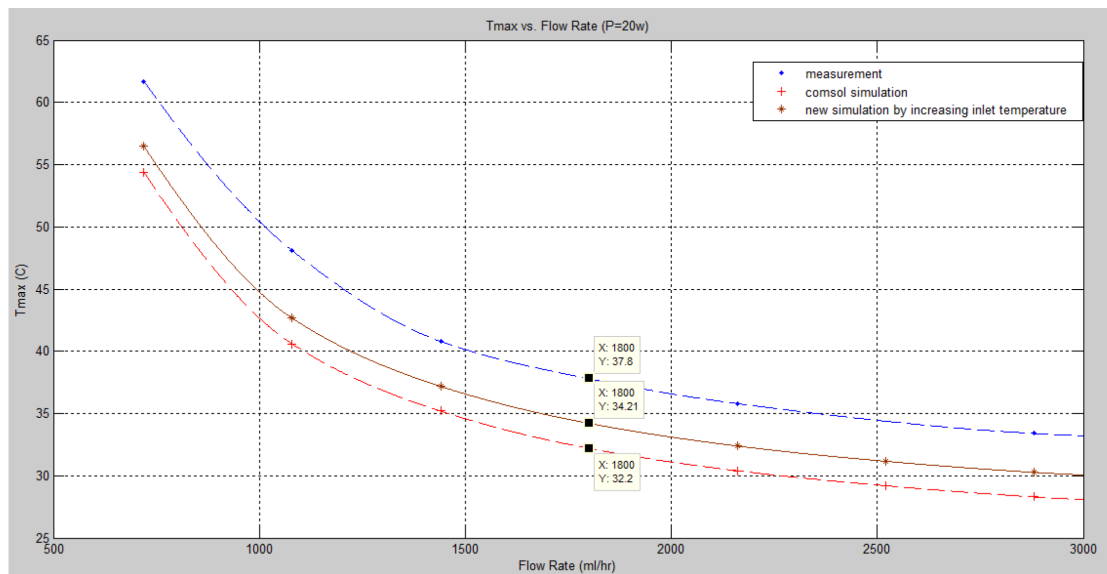

Figure 5.7- The measured maximum surface temperature for the 5-channel cooling device as a function of the flow rate for a dissipated power of 20W compared to new FEM simulations.

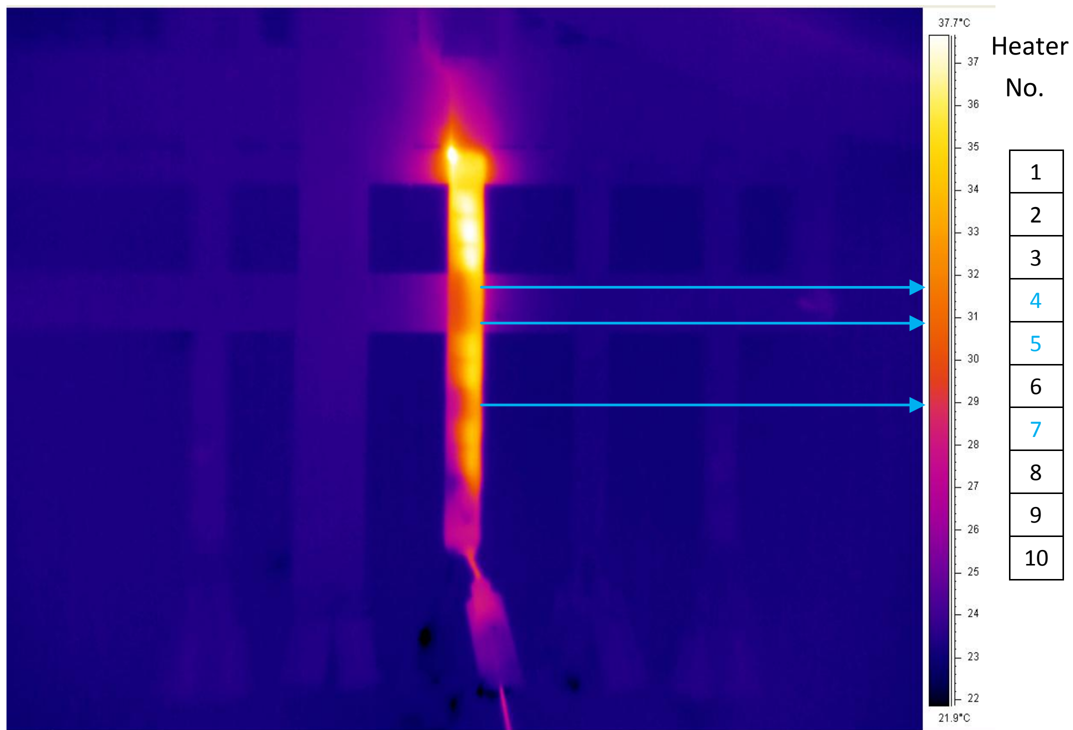

Figure 5.8- The surface temperature distribution image measured by infra-red camera on the 5-channel cooling device for a dissipated power of 20W and flow rate at 1800ML/hr.

After testing and verifying the cooling capability of the 5-channel device, the cooling capacity of the other four chips with different contact surface areas was investigated. Because of the current HIFU device specification, the best measurement way is to directly test and compare results for the different chips at a power dissipation of 20W on 10 heaters. Unfortunately, due to the fact that on some of the devices the some of the heaters were broken, it was not possible to make this comparison directly. Due to the limited time available, the new test samples are not used in this experiment. Table 5.1 shows the position of broken heaters for different micro-channel devices. In an alternative measurement the devices were operated with only two heaters (no. 1&2) at a lower power level of 6 W.

Under microscope, there are two types of visual defects on the devices. First, part of silicon on the 2-channel chip (“x”) is missing. As shown in the Fig 5.9 (A), the missing silicon which is placed between heaters and bond pads can cause the three aluminum interconnections fail. Therefore the last three heaters of that chip cannot work functionally (no. 8-10). This missing silicon usually is the result of the dicing process. In addition, Fig. 5.9 (B) shows the reason why the no.4 heater (“x”) on 5-channel chip is broken. According to the optical image (Fig 5.9 (B)), there are some scratches on the aluminum track, which result the aluminum disappearing on that position. Because of this, the no.4 heater of 5-channel chip is broken.

Except these two defects, the problem of the broken three heaters of 9-channel device and no.8 heater of 5-channel device ("x") is the disconnection between their macroscopic connectors and the PCB. This problem is solved by using more soldering to get a proper jointing. For the rest two nonfunctional heaters ("x"), there are no apparent visual defects or soldering connection problem. One possible explanation for them is the electrical wire bonding problem.

Table 5.1- Position of broken heaters in four types of test cooling devices

No.	1	2	3	4	5	6	7	8	9	10
2-channel								x	x	x
3-channel			x							
5-channel				x	x			x		
9-channel						x	x	x		

▪ "x" presents a broken heater. The different colors of x means the different reasons which cause the heater cannot work functionally.

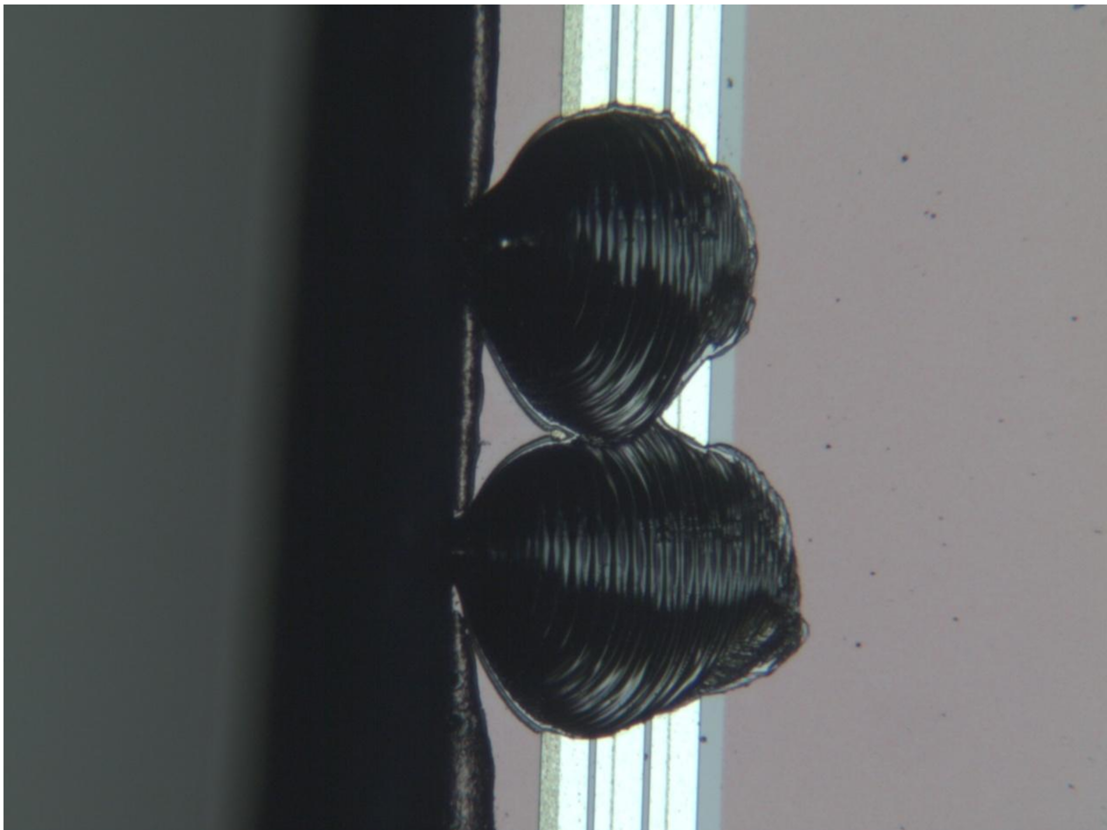

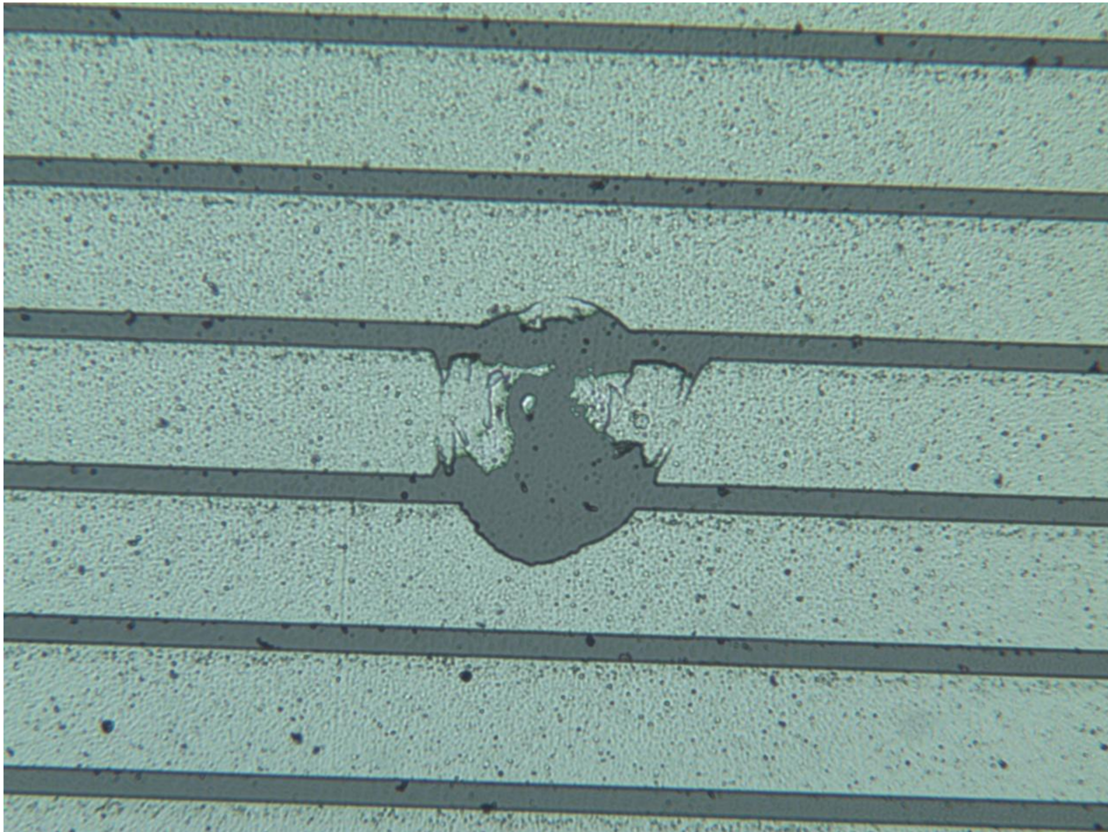

Figure 5.9- Optical images of detects found on heaters due to the different reasons. (A) the missing silicon; (B) the scratches of aluminum pattern

At a dissipation power of 6W, the measured result is shown in Tab. 5.2 and Fig. 5.9. In the graph, there are two contradictory conclusions for different flow ranges. In the high flow rate range (>2000 mL/hr), the 9-channel chip demonstrated the best cooling capacity. However, in low flow rate range (<1500 mL/hr), the performance of 9-channel chip is the worst one. To avoid the measurement error, this test has been carried out three times at lowest flow rate (720mL/hr) and highest flow rate (2880mL/hr).

Table 5.2- The maximum surface temperature vs. different flow rates

Q_{enter} (mL/hr)	$Q_{measured}$ (mL/hr)	T_{max} (°C) 9-channel	T_{max} (°C) 5-channel	T_{max} (°C) 3-channel	T_{max} (°C) 2-channel
1000	720	50.1	43.8	42.6	42
1500	1080	40	37.6	37.8	37.9
2000	1440	35.7	35	35.6	35.9
3000	2160	32.4	32.6	33.4	33.9
4000	2880	30.5	31.6	32.1	32.6

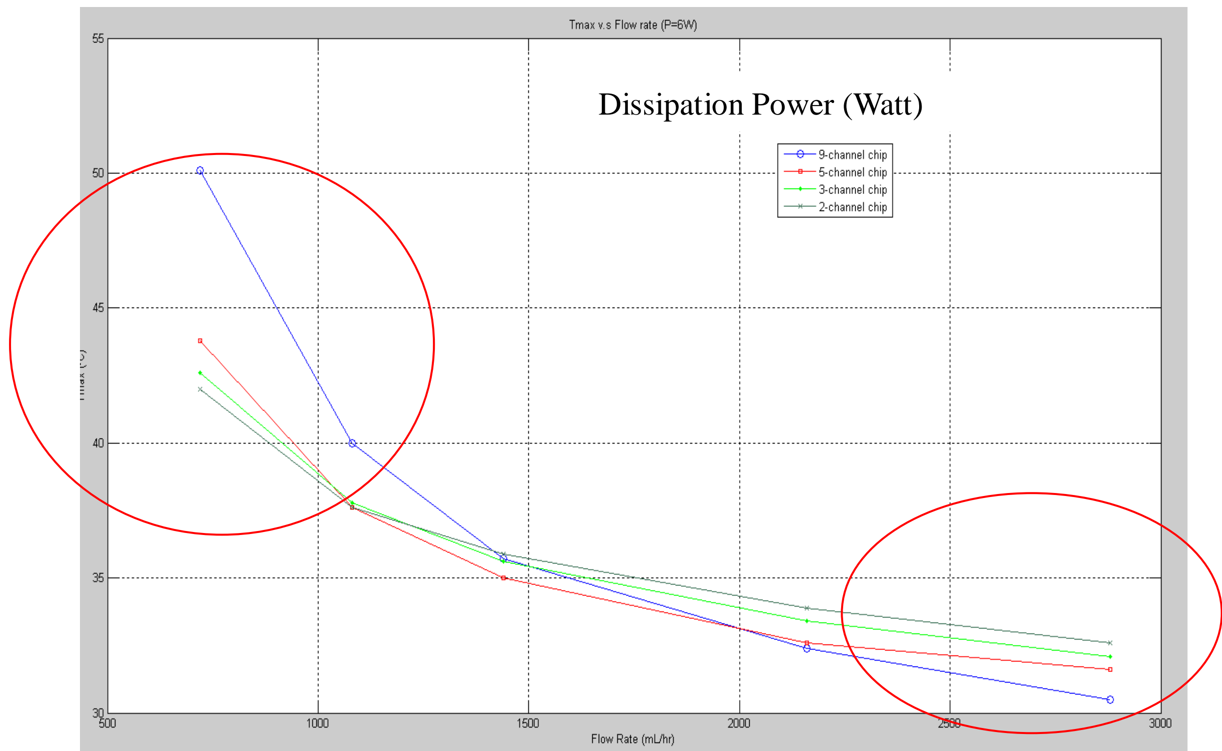

Figure 5.10- max surface temperature on the four types of cooling device as a function of the flow rate for a dissipation power of 6W.

Since lacking enough theoretical knowledge and equations for U-shaped micro-channels, the analysis and explanation for Fig. 5.10 are not fully confirmed. There are two main possible explanations for the results. The heat transfer equation is defined as, [21]

$$q = h * A * \Delta T$$

where q is heat flow [W], h is heat transfer coefficient [W/(m^{2}K)], A is heat transfer surface area [m^2], and ΔT is difference in temperature between the solid surface and surrounding fluid area [K].

From this equation it can be seen that the maximum surface temperature depends on both transfer surface area (A) and heat transfer coefficient (h).

Several investigations and experiments show, that for micro channels, the transition from laminar to turbulent flow occurs at much smaller Reynolds numbers than for normal size channels. For example, Peng et al. (1994) and Peng and Peterson (1996) reported that the conversion from the laminar to the transition regime occurred at Re=200-700[23-24]. In our test, at a flow rate of 720 mL/hr, the Reynolds number of 9-channel chip is just 91 so that a laminar flow can be assumed. But the Reynolds number of 2-channel chip is 281, it is therefore possible that for this device the flow is in the transition region which can generate a higher transfer coefficient and lead to a better cooling capacity than 9-channel device. Additionally in the high flow rate range, all the water flows in the different devices start to be in the transient range. As a result the influence of heat coefficient is reduced and the heat transfer contact surface area

becomes the critical impact element for the different cooling devices. When the heat transfers for different test cooling devices are constant or similar, the 9-channel cooling device with a larger heat transfer surface area can have a better cooling capacity, which corresponds to the observations in the high flow rate ranges.

Another possible reason for the observations in Fig. 5.10 is a blockage of one of the micro-channels. With the smallest width of channel, some micro channels in the 9-channel chip have more opportunities to be blocked by glue or particles. This also results in a reduction of heat transfer surface area which means a worse cooling capacity. Unfortunately, after sealing the device, it is impossible to observe each micro channel inside the cooling chip which means that this assumption can't be confirmed at this moment.

Next, a pressure sensor is implemented to measure the pressure drop on the inlet port of 5-channel devices as a function of flow rate. Due to the limited sensor range, the results are only measured at the low flow rate range. Fig 5.11 shows the pressure drop has a linear relationship with flow rate in the rectangle micro-channels as expected in Section 2.2.3.

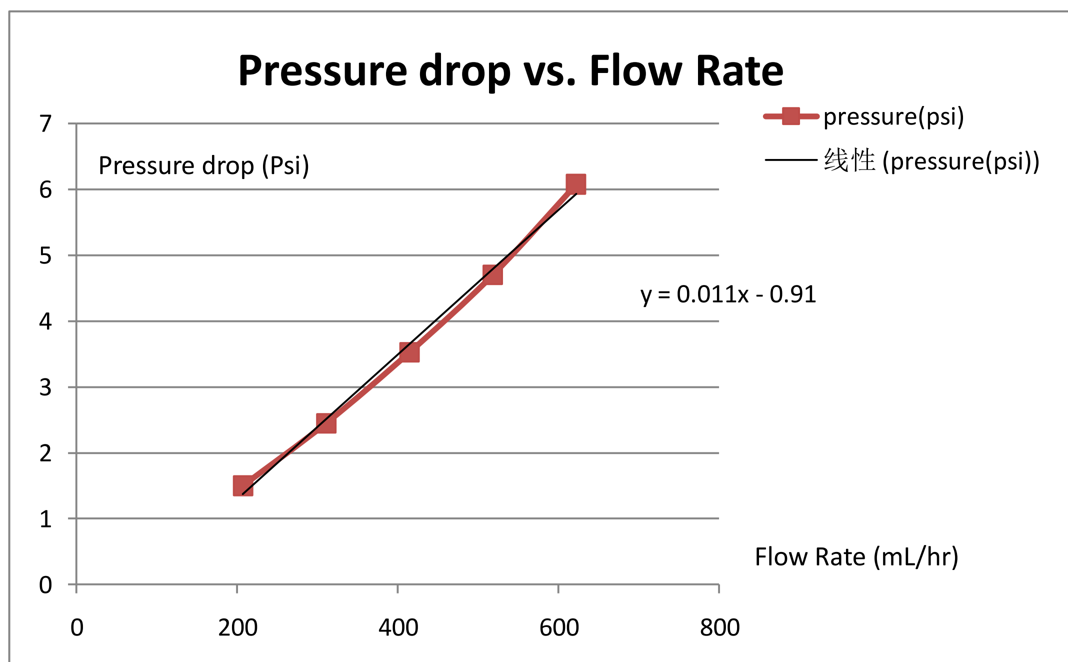

Figure 5.11- Pressure drop on the inlet port of 5-channel device as a function of flow rate

5.2 MRI guide HIFU experiments

As mentioned in Chapter 1, an important HIFU application is MRI-guided HIFU. Figure 5.12 demonstrates an existing MRI-guided HIFU system in the Philips Sonalleve MR-HIFU. It combines the power of two modalities by integrating an advanced High Intensity Focused Ultrasound system into the patient table of the

Philips Achieva MR system [20].

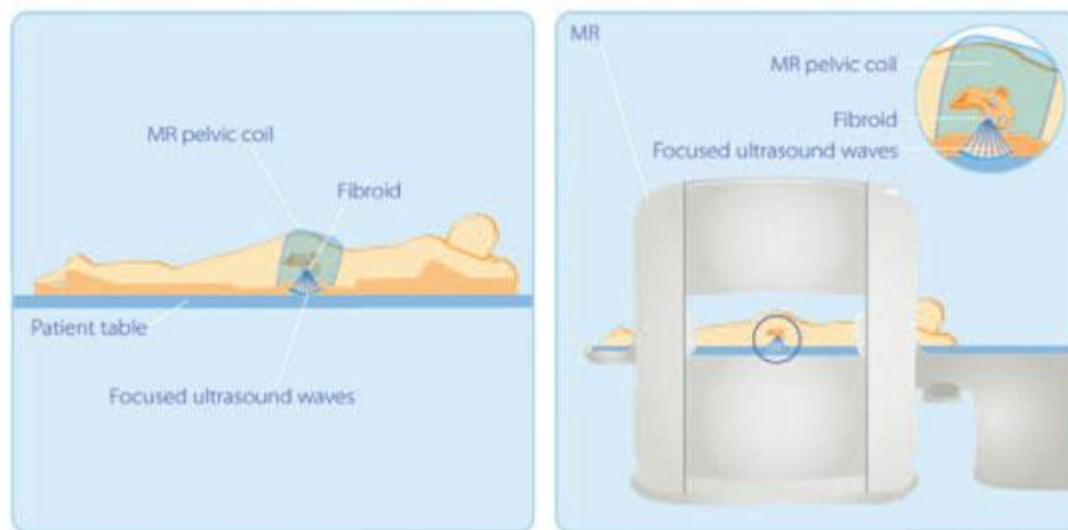

Figure 5.12- Sonalleve treatment of uterine fibroids

For these mature MRI-HIFU systems, the HIFU devices are integrated in the table, outside the human body. For guiding and monitoring of HIFU ablation, MRI offers clear advantages over other imaging modalities.

For future HIFU ablation catheters inside the body, the MRI imaging quality is still one of critical impact factors. And therefore, a new MRI compatibility test was carried out. In order to observe the MR-HIFU image quality, the “real cooling device”, is scanned under different imaging parameters. During the experiment, the real cooling device is placed inside highly hydrated or water-rich gels which provide similar conditions like human tissue, and scanned with the Philips Achieva 3.0T system (Fig. 5.13).

All the MRI images are presented in the Fig. 5.14. By applying different echo times (TE) and changing the angels of the sample in the gel, the MRI results are clear enough to distinguish the cooling device from surrounding gels. It means the future silicon HIFU chip still could be integrated with MRI system without resulting in many artifacts.

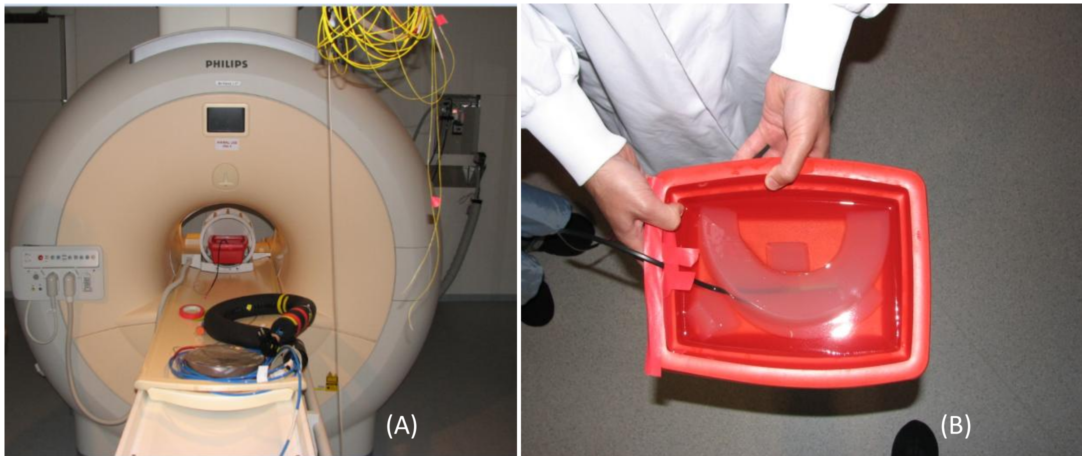

Figure 5.13-(A) Philips Achieva 3.0T system
(B) Real Cooling Device placed inside the gels

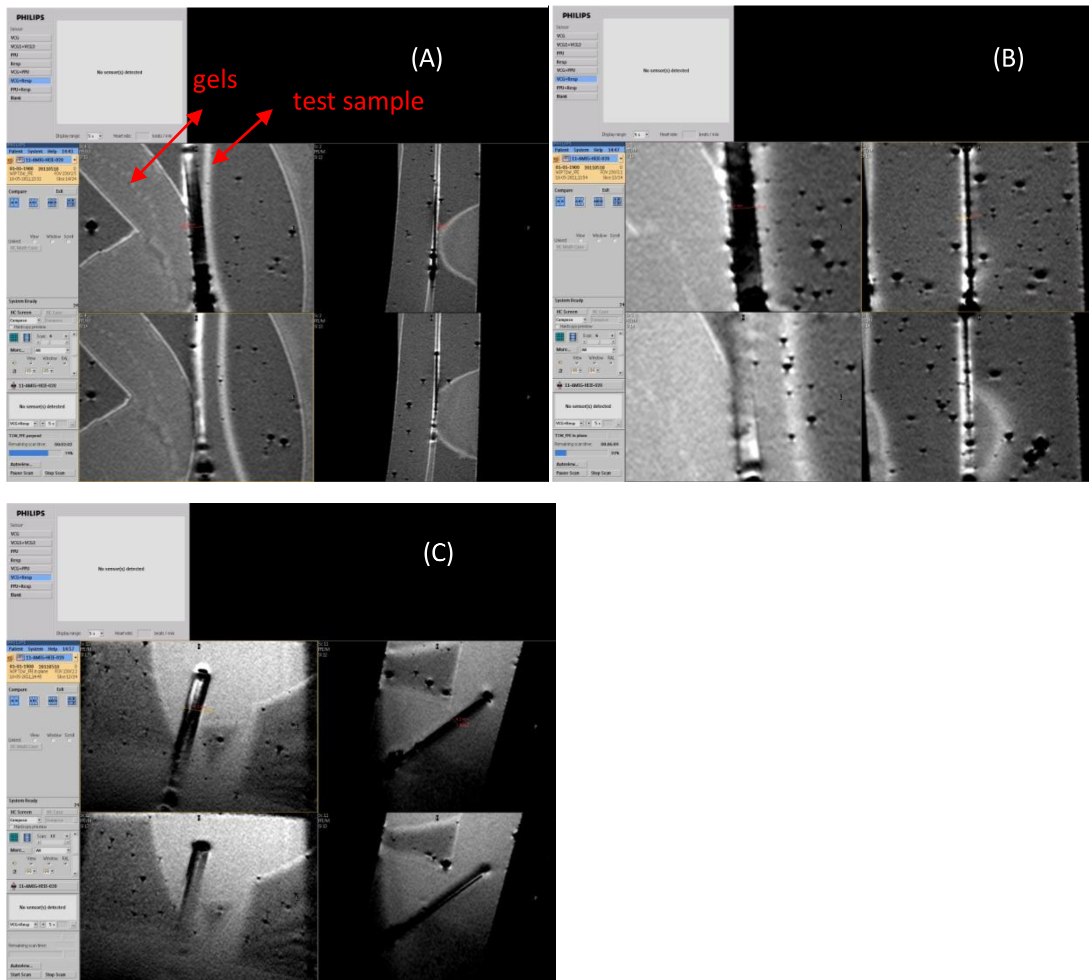

Figure 5.14-(A) Gradient echo (FFE) of test device between gels TE = 4.4 ms
(B) Gradient echo of test device between gels TE = 20 ms
(C) Gradient echo of test device under an angle 30 approximately degrees TE= 20 ms

Chapter 6 Conclusions and recommendations

In this thesis the possibility to integrate water cooling for an HIFU prostate ablation device was investigated. The water cooling uses micro channels etched in the backside of the silicon wafers on which the HIFU devices are fabricated. In this investigation, the HIFU devices are replaced by aluminum heaters since the fabrication of these devices is rather complicated. In total ten heaters are used to mimic the layout of the real HIFU device which also has ten transducers. In total the ten heaters should be able to dissipate 20 Watt with a maximum surface temperature of only 42℃.

Two types of device were designed. The first type called “ the real cooling device” was designed to be mounted on the end of a catheter. It has the fluidic and electrical connections on the same end. The second type called “the test cooling device” was designed to fascilitate testing of the device. It has the electrical connections on one end of the device, and the fluidic connections on the other end. In this way the device could be easily mounted on a Printed Circuit Board (PCB) in such a way that the electrical wire-bonds were not in the way of the fluidic tubes and visa versa.

In order to explore the relationship between the cooling capacity and the heat transfer contact surface area, four different numbers of the micro channels are designed. The devices are designed to have the same cross sectional area, but differ in their contact surface area. FEM simulations were used to obtain a visual impression on the surface temperature distribution and an approximation of the maximum surface temperature as a function of flow rate and dissipated power.

Measurements show that even with a moderate water flow of 1440 ml/hr it is possible dissipate 20 Watt of power without the surface temperature of the device exceeding 42℃. Unfortunately a direct comparison of the devices with different surface contact areas was not possible since some of the heaters were damaged during the assembly process.

The “real cooling device” was mounted on the tip of a catheter, and tested in a real MRI setup. The MRI images obtained showed no artifacts, demonstrating the MRI compatibility of the device.

Although most the micro channels of most of the test devices were sealed by gluing “a mirror device” back-to-back to it, the possibility to use wafer scale BCB bonding was also successfully explored. In this case a glass wafer was bonded to the silicon wafer to allow for visual inspection after bonding.

Recommendations for future work:

(1). Prepare the perfect four types of test devices without broken heaters and redo the cooling capacity test at 20 Watt again to find a more reliable relationship between the maximum surface temperature and transfer surface area, especially at low flow rate range.

(2). Implement a pressure sensor with a suitable range to measure the pressure drop on the inlet port of devices.

(3). For new test mask the devices should be designed with mirror symmetry to allow for proper BCB bonding.

(4). The shape of micro channels should be optimized to reduce the pressure drop. This can for instance be done by rounding the sharp corners of U-turn part.

(5). By decreasing the width of the micro-channels and increasing their number, the heat transfer area can be increased. The effects on cooling capacity and pressure drop should be explored.

(6). Increasing the height of micro channel, will increase the heat exchange area and result in a better cooling capacity at high flow rates. However, this also results in a thinner silicon diffuser layer and additionally the devices may become more fragile. As a result the optimal channel height will need to be determined.

(7). In further FEM simulations the vacuum of the surrounding environment should be replaced by air and water to obtain a more realistic simulation result.

Reference

[1]. National Cancer Institute (NCI) booklet, “What you need to know™ about Prostate Cancer”
“http://www.cancer.gov/cancertopics/wyntk/prostate/allpages#ab3d4f20-6ab9-4428-9717-067035d2e691”.

[2]. National Cancer Institute at the National Institutes of Health, “Prostate Cancer Treatment”, http://www.cancer.gov/cancertopics/pdq/treatment/prostate/Patient.

[3]. Kevin C. Zorn, MD, FACS, FRCSC, and Gagan Gautam, MD, MCh, “Prostate Cancer”, “http://www.medicinenet.com/prostate_cancer/article.htm”.

[4]. Medical News Today, “What Is Prostate Cancer? What Causes Prostate Cancer?”, “http://www.medicalnewstoday.com/articles/150086.php”.

[5]. Kennedy JE, Ter Haar GR, Cranston D, “High intensity focused ultrasound: surgery of the future?”, British Journal of Radiology (2003) 76, pp. 590-599

[6]. Watkin, N.A, ter Haar, G.R., R. Marsden Hospital, Sutton, “High intensity focused ultrasound: applications in urology”, *Technological Advances in Therapeutic Urology, IEE Colloquium*, 23 Apr 1996, pp. 4/1 - 4/3.

[7]. H.Azzouz, J.J.M.C.H.de la Rosette, “*EAU-EBU Update Series*, Volume 4, Issue 2, April 2006, pp. 62-70.

[8]. Chrit Moonen, “MRI-guided high intensity focused ultrasound (HIFU)”.

[9]. Wikipedia, “Prostate Cancer”, “http://en.wikipedia.org/wiki/Prostate_cancer”.

[10]. Frank P. Incropera, David P. Dewitt, “Fundamentals of Heat and Mass Transfer, 5th Edition”.

[11]. John H. Lienhard IV, John H. Lienhard V, “A Heat Transfer Textbook”.

[12]. Wikipedia, “Convection”, “http://en.wikipedia.org/wiki/Convection”.

[13]. Remco Pijnenburg, “ Integrated cooling in silicon”, master thesis.

[14]. “Low Reynolds number flows”,
“http://www.docstoc.com/docs/13373488/Low-Reynolds-number-flows”.

[15]. Wikipedia, “Hydraulic diameter”,

"http://en.wikipedia.org/wiki/Hydraulic_diameter"

[16]. N.T. Nguyen, "Micromixers: Fundamentals, Design and Fabrication", William Andrew, 2008.

[17]. J. P. Holman, "Heat Transfer, Tenth Edition".

[18]. Satish G. Kandlikar, "Heat transfer and fluid flow in minichannels and microchannels"

[19]. Wikipedia, "Sheet resistance", "http://en.wikipedia.org/wiki/Sheet_resistance".

[20]. T. Gessner and T. Otto and M. Wiemer and J. Frömel, "Wafer bonding in micro mechanics and microelectronics - an overview". T*he World of Electronic Packaging and System Integration, The World of Electronic Packaging and System Integration,* pp. 307-313.

[21], Xiaodong Zhou, Selven Virasawmy, Chenggen Quan, "Wafer-level BCB bonding using a thermal press for microfluidics", *Microsystem Technologies*, Volume 15, Number 4, pp. 573-580,

[22]. Dow, "Processing Procedures for Dry-Etch CYCLOTENE Advanced Electronics Resins (Dry-Etch BCB)".

[23]. Wikipedia, "Heat transfer coefficient", "http://en.wikipedia.org/wiki/Heat_transfer_coefficient".

[24]. X. F. Peng, G. P. Peterson, "Heat Transfer characteristic of water flowing through microchannels", *Experimental Heat Transfer*, Volume 7, Issue 4, 1994

[25]. Hao Li and Michael G. Olsen, "Examination of large-scale structures in turbulent microchannel flow", *Experiments in Fluids,* Volume 40, Number 5, pp. 733-743,

[26]. Gophinath R. Warrier, Vijay K. Dhir and Lesile A. Momoda, "Heat transfer and pressure drop in narrow rectangular channels", *Experimental Thermal and Fluid Science*, Volume 26, Issue 1, April 2002, pp. 53-64

[27]. Philips, "Sonalleve MR-HIFU", "http://www.healthcare.philips.com/main/products/mri/systems/sonalleve/index.wpd"

Acknowledgment

I am heartily thankful to my supervisor Prof. Ronald Dekker for his encouragement, guidance and support from the initial to the final level. Without his knowledge, advice and leadership, it is not possible to finish this project.

I also offer my regards and blessings to other Philips colleagues and clean room staff at Miplaza for their assistance in fabrication processes. During the clean room work, they provided me a lot of useful assistance.

I gratefully thank everyone at the student room in the Micro System & Device Department during this project. A special thank goes to Angel Savov for his help on various aspects of the project. The discussions with him have been exceptionally helpful and inspiring.

At last but not the least, I would like to express my thanks to all my family and my friends for their support all this time.

Appendix A- Detailed fabrication sequence

- **Prepare wafers from stock**
  - Substrates 150mm, 20Ω·cm <100> monocrystalline silicon with 0.5μm thermal oxide
  - Chemical mechanical polishing the backside
  - Clean: (1), in the Cintillio; recipe: to remove organic rest (HZplus18min); (2), in the Cintillio; recipe: standard cleaning (FZplusHCL)
  - Wet etch 10 min for 0.5μm of oxide in BOE until hydrophobic

- **Oxidation steps**
  - Clean in the Cintillio; recipe: standard cleaning (FZplusHCL)
  - 1μm of thermal oxide at 1000 °C growth
  - 2μm of PECVD oxide deposited on the backside at 350 ℃ in Novellus

- **Patterning of the backside oxide layers**
  - Clean: (1), Cintillio; recipe: to remove organic rest (Hzplus30min) (2), in the Cintillio; recipe: standard remove (FZplusHCL)
  - Spin coat 2.8 μm HPR504@1000rpm+TMSDA on the backside of wafer on ACS track
  - Expose CBB mask on MA-8 Karl Suss contact aligner for 20 seconds
  - Develop HPR504 on ACS track
  - Rinse in DI water to remove the remnants of developer from the backside
  - Etch 3 μm of oxide on Applied Precision 5000
  - Descum in oxygen plasma barrel: 90 ℃, 7 minutes. Then twice acetone strip the resist on backside side on the ACS track.
  - Clean: (1), in the Cintillio; recipe: to remove organic rest (HZplus18min); (2), in the Cintillio; recipe: standard cleaning (FZplusHCL)

- **Fabrication of the heater structures on the frontside**
  - Sputter 0.7 μm aluminum on the frontside--no sputter etch
  - Spin coat HPR504 @ 4000 rpm on the frontside of wafer on ACS track
  - Expose IN mask on MA-8 Karl Suss contact aligner for 20 seconds
  - Develop HPR 504 on ACS track
  - Rinse in DI water to remove the remnants of developer from the frontside
  - Bake on 90 in the oven for half an hour to make resist weak
  - Wet etch the aluminum in PES for 7 minutes

- Acetone strip the resist on the frontside on the ACS tracks
- Cleaning in fuming HNO_3 for 10 minutes
- Deposit 0.7 µm of PECVD nitride (Si_3N_4)
- Spin coat 1.3 um HPR504 @ 2000 rpm + TMSDA on the frontside of wafer on the ACS track
- Expose CO mask on MA-8 Karl Suss contact aligner for 10 seconds
- Develop HPR504 on ACS track
- Dry etch nitride
- Resist strip in oxygen plasma barrel 1000 W, 130 ℃, 45minutes

- **DRIE etching of the micro-channels**
  - DRIE etching for 500 µm (anisotropic) on the backside of wafers
  - Bake the wafer in the oven for 30 minutes to remove passivation polymer

Appendix B- Detailed process flow of BCB wafer bonding

1. BCB roller transfer (flexible substrate and silicon wafer)

1.01. Descum invar foil in the Barrel IPC 9200, O_2-110 ℃-600Watt-5min.

1.02. Spin coat BCB 3022-46 on invar in the RC8 MS3 Gyrset, disp.5ml 30s@100rpm, sprd 15s@500rpm,spin 30s@1000rpm lid open

1.03. Soft bake invar foil on the hot plate, T=95 ℃, t=3min

1.04. Mounting invar foil on the roller

1.05. Descum silicon wafer in Barrel IPC 9200, O_2-110 ℃-600Watt-5min.

1.06. Put silicon wafer on hotplate, t=20 sec, T=100 ℃ and setpoint of hot plate is 103 ℃

1.07. Roll transfer, 3mm/sec

1.08. Reflow-bake on hotplate, t=15min,T=150 ℃

1.09. Visual inspection

2. Bonding silicon wafer on glass wafer

2.01. Descum glass wafer in the Barrel IPC 9200, O_2-110 ℃-600Watt-5min

2.02. Rinse and spindry in the Verteq

2.03. Spincoat AP3000 in the Convac, disp.5ml 30s@100rpm,sprd 15s@500rpm,spin 30s@1000rpm lid open

2.04. Bake in the Heraeus oven at T=125 ℃, t = 15min

2.05. Wafer stack alignment of silicon-glass wafers on SÜSS MicroTec, with spacer gap 100 µm, program 13, B-TRE-ME1

2.06. Wafer bonding of silicon-glass wafers in SB 6 SÜSS MicroTec, with graphite and Al foil, program BCB_Philips3 (Fig.1).

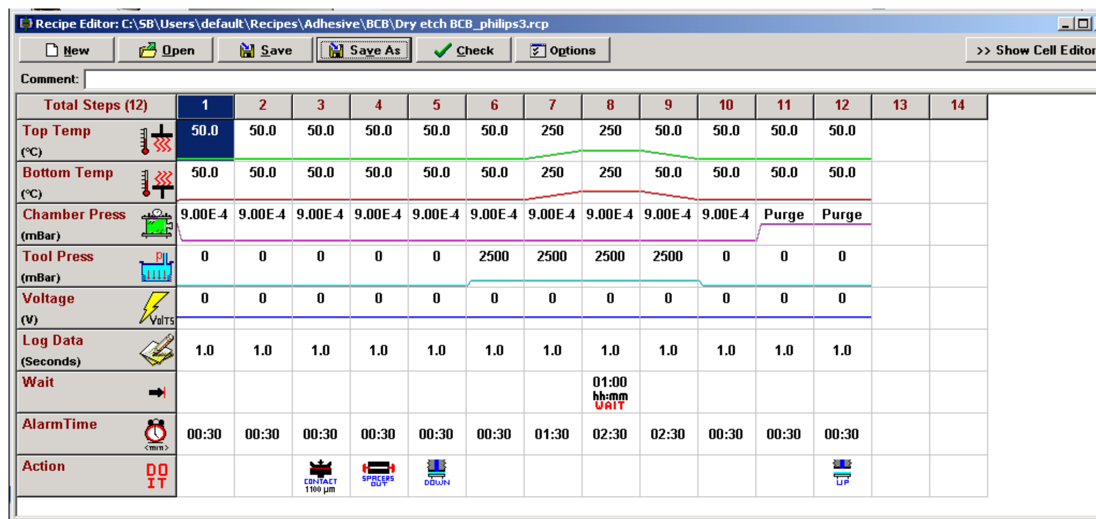

Recipe Editor: C:\SB\Users\default\Recipes\Adhesive\BCB\Dry etch BCB_philips3.rcp

New | Open | Save | Save As | Check | Options | >> Show Cell Editor

Comment:

Total Steps (12)	1	2	3	4	5	6	7	8	9	10	11	12	13	14
Top Temp (°C)	50.0	50.0	50.0	50.0	50.0	50.0	250	250	50.0	50.0	50.0	50.0		
Bottom Temp (°C)	50.0	50.0	50.0	50.0	50.0	50.0	250	250	50.0	50.0	50.0	50.0		
Chamber Press (mBar)	9.00E-4	9.00E-4	9.00E-4	9.00E-4	9.00E-4	9.00E-4	9.00E-4	9.00E-4	9.00E-4	9.00E-4	Purge	Purge		
Tool Press (mBar)	0	0	0	0	0	2500	2500	2500	2500	0	0	0		
Voltage (V)	0	0	0	0	0	0	0	0	0	0	0	0		
Log Data (Seconds)	1.0	1.0	1.0	1.0	1.0	1.0	1.0	1.0	1.0	1.0	1.0	1.0		
Wait								01:00 hh:mm WAIT						
AlarmTime	00:30	00:30	00:30	00:30	00:30	00:30	01:30	02:30	02:30	00:30	00:30	00:30		
Action			CONTACT 1100 µm	SPACERS OUT	DOWN							UP		

Figure 1- Program BCB_Philips 3